

Mass Hierarchy determination via future Atmospheric Neutrino Detectors

Raj Gandhi ^{a,*}, Pomita Ghoshal ^{a,†}, Srubabati Goswami ^{a,‡}, Poonam Mehta ^{b,§},
S Uma Sankar ^{c,¶}, Shashank Shalgar ^{a,||}

^a Harish-Chandra Research Institute, Chhatnag Road,
Jhansi, Allahabad 211 019, India

^b Department of Particle Physics, Weizmann Institute of Science,
Rehovot 76 100, Israel

^c Department of Physics, Indian Institute of Technology, Powai,
Mumbai 400 076, India

Abstract

We study the problem of determination of the sign of Δm_{31}^2 , or the neutrino mass hierarchy, through observations of atmospheric neutrinos in future detectors. We consider two proposed detector types : (a) Megaton sized water Čerenkov detectors, which can measure the event rates of $\nu_\mu + \bar{\nu}_\mu$ and $\nu_e + \bar{\nu}_e$ and (b) 100 kton sized magnetized iron detectors, which can measure the event rates of ν_μ and $\bar{\nu}_\mu$. For energies and path-lengths relevant to atmospheric neutrinos, these rates obtain significant matter contributions from $P_{\mu e}$, $P_{\mu\mu}$ and P_{ee} , leading to an appreciable sensitivity to the hierarchy. We do a binned χ^2 analysis of simulated data in these two types of detectors which includes the effect of smearing in neutrino energy and direction and incorporates detector efficiencies and relevant statistical, theoretical and systematic errors. We also marginalize the χ^2 over the allowed ranges of neutrino parameters in order to accurately account for their uncertainties. Finally, we compare the performance of both types of detectors vis a vis the hierarchy determination.

PACS: 14.60.Lm,14.60.Pq,13.15.+g,29.40.Ka,29.40.Vj

* raj@mri.ernet.in

† pomita@mri.ernet.in

‡ sruba@mri.ernet.in

§ poonam.mehta@weizmann.ac.il

¶ uma@phy.iitb.ac.in

|| shashank@mri.ernet.in

1 Introduction

Our understanding of neutrino physics has progressed impressively over the last decade owing to outstanding results from solar, atmospheric, reactor and accelerator based neutrino oscillation experiments. For three neutrino flavors, the picture of neutrino masses and mixings emerging from these results is:

- There are two independent mass squared differences ¹ given by $|\Delta m_{31}^2| \sim 10^{-3} \text{ eV}^2$ and $\Delta m_{21}^2 \sim 10^{-5} \text{ eV}^2$;
- Of the three mixing angles, two (θ_{12} and θ_{23}) are large, while the third mixing angle (θ_{13}) is small and constrained only by an upper bound.

In Table 1, we summarize the present bounds (the best-fit values and 3σ ranges) of these parameters.

Parameter	Best-fit value	3σ range
$\Delta m_{21}^2 [10^{-5} \text{ eV}^2]$	7.9	7.1 – 8.9
$ \Delta m_{31}^2 [10^{-3} \text{ eV}^2]$	2.5	1.9 – 3.2
$\sin^2 \theta_{12}$	0.3	0.24 – 0.40
$\sin^2 \theta_{23}$	0.5	0.34 – 0.68
$\sin^2 \theta_{13}$	0.0	≤ 0.041

Table 1: Best-fit values and 3σ allowed intervals for three-flavour neutrino oscillation parameters from combined analysis of global data including solar, atmospheric, reactor (KamLAND and CHOOZ) and accelerator (K2K and MINOS) experiments [1].

These results have also delineated the main goals of neutrino oscillation research over the next decade, which can be summarized as follows :

- Improved precision on the mass squared differences (Δm_{21}^2 and Δm_{31}^2) and the mixing angles (θ_{23} and θ_{12}) ;
- Determination of θ_{13} , especially ascertaining if its value is non-zero ;
- Determination of $\text{sign}(\Delta m_{31}^2)$ or the hierarchy of neutrino masses ;
- The presence, or otherwise, absence of CP violation in the leptonic sector and the value of the phase δ_{CP} .

¹We use the convention $\Delta m_{ji}^2 \equiv m_j^2 - m_i^2$.

The experimental realization of the above goals is a complex task. Hence, a large number of neutrino experiments are being constructed or being planned to work towards achieving these aims.

Our focus in this work is to bring out the potential of megaton water Čerenkov detectors (*e.g.* HK [2, 3], UNO [4] or MEMPHYS [5]) and magnetized iron detectors (*e.g.* INO [6]) vis a vis the goal of determining the neutrino mass hierarchy. Both of these detector-types plan to use atmospheric neutrinos as one of their primary sources. Each category of detector has a special ability, in addition to large statistics resulting from its massive size. In the case of water Čerenkov detectors, one can detect both muons and electrons, whereas in the case of magnetized iron detectors, it is possible to study muons and anti-muons separately by charge discrimination. These advantages, together with their size, and the wide ranges in energy and path-length made available by atmospheric neutrinos, make these detectors powerful tools for studying $\text{sign}(\Delta m_{31}^2)$.

Solar neutrino data require Δm_{21}^2 to be positive. However, data from atmospheric neutrino experiments as well as accelerator neutrino experiments (K2K and MINOS) constrain only the magnitude of Δm_{31}^2 but not its sign. If $\text{sign}(\Delta m_{31}^2) > 0$, then we have the mass pattern, $m_3 \gg m_2 \gg m_1$, which is similar to that of the charged leptons. This is called the normal hierarchy (NH). If $\text{sign}(\Delta m_{31}^2) < 0$, then the mass pattern is $m_2 \geq m_1 \gg m_3$. This is called the inverted hierarchy (IH). These statements, of course, are meaningful provided a discernible and non-trivial hierarchy exists among the neutrino mass eigenstates, or, in other words, the lightest neutrino state is almost massless. If future experiments on tritium beta decay or neutrinoless double beta decay show that the absolute scale of neutrino masses is, for instance, $\gtrsim 0.3$ eV, then all three neutrino masses must be nearly degenerate. However, one may still ask the question if $\text{sign}(\Delta m_{31}^2)$ is positive or negative.

Attempts to construct unified theories beyond the Standard Model depend crucially on the hierarchy. In fact, one way to classify families of unification models is via the hierarchy they assume as input. It is thus an important ingredient in our quest for a unified theory, and its determination would in essence eliminate or strongly disfavour large classes of such theories and considerably narrow the focus of this search.

Generally speaking, determination of the mass ordering in oscillation experiments requires the observation of measurably large matter effects (*i.e.* long baselines) and a not too small value for $\sin^2 2\theta_{13}$ ($\gtrsim 0.05$). This limits the sensitivity of presently planned superbeam experiments to hierarchy determination as the baselines involved are moderate ($\lesssim 800$ km) and significant matter effects do not develop. Also at these baselines, for the $P_{\mu e}$ channel which these experiments use, the oscillation probability depends jointly on three unknown parameters: $\text{sign}(\Delta m_{31}^2)$, the phase, δ_{CP} and the mixing angle, θ_{13} . This results in a ($\delta_{\text{CP}}, \text{sign}(\Delta m_{31}^2)$) degeneracy where acceptable solutions corresponding to the two signs of Δm_{31}^2 can appear at different values of δ_{CP} and θ_{13} [7]². To overcome this problem, the synergistic use of two experiments [13–18] or two detectors at different baselines [19, 20] has been suggested. Among the combinations studied, the planned superbeam experiments T2K [21, 22] and the NuMI Off-axis experiment NO ν A [23] may be able to infer the neutrino mass hierarchy [24–27].

²The δ_{CP} dependence tends to decrease for longer baselines, and in fact vanishes at (and around) the so called “magic baseline” (~ 7000 km) [8–12], reappearing subsequently at longer baselines.

In this paper, in order to ascertain the neutrino mass hierarchy, we focus on the appreciable resonant matter effects encountered by atmospheric neutrinos with energies between 2–10 GeV which traverse distances between 4000–12500 km inside the earth. Until very long baseline experiments using β -beams or neutrino factories are built atmospheric neutrinos are the only source that permit us to exploit these spectacular effects [11, 28–33]. Moreover, for these energy and pathlength ranges, it turns out that the effects of δ_{CP} degeneracy are not very significant [34]. Therefore, lately, the subject of hierarchy determination using atmospheric neutrinos has received considerable attention [34–39]. Recent work has also emphasized the degeneracy resolving power of atmospheric neutrino data [40–42] in the context of water Čerenkov and magnetized iron detectors respectively. In particular, the issue of the resolution of $(\theta_{23}, \pi/2 - \theta_{23})$ degeneracy in magnetized iron detectors has been considered in [43, 44].

In our earlier work on this subject [34, 45] we had used the total event count rates (in the energy range 2–10 GeV and pathlength range 4000–10000 km) to examine the determination of the neutrino mass hierarchy for iron magnetized calorimeters and water Čerenkov detectors respectively. Since we used total event rates, the effects of energy and angular smearing were not very important in those analyses. We had also made the simplistic assumption that the values of the neutrino parameters are known exactly. In this paper, we relax this assumption and take into account the uncertainties in the determination of neutrino oscillation parameters. Under these circumstances, the total event rates can no longer give good sensitivity and therefore one has to do a binned spectrum analysis including appropriate angular and energy smearing. In what follows, we do a detailed study of the effect of these refinements on the hierarchy sensitivity for both water Čerenkov and iron calorimeter detectors.

The hierarchy sensitivity of iron calorimeter detectors was studied in [38] under the approximation that $\Delta m_{21}^2 = 0$. In our numerical work we take Δm_{21}^2 to be non-zero because, in principle, it becomes important in the limit of small θ_{13} . However, the marginalization over $|\Delta m_{31}^2|$ washes out the hierarchy sensitivity due to non-zero Δm_{21}^2 in this limit. Allowing a non-zero value for Δm_{21}^2 allows us to study the variation of χ^2 with δ_{CP} . We also compare and contrast the performance of a magnetized iron calorimeter detector with a water Čerenkov detector in discriminating between the two hierarchies.

In the next section, we discuss and summarize the matter sensitivities of various oscillation probabilities that are relevant to the atmospheric neutrino signal and give analytic expressions for maximum hierarchy sensitivity. Section 3 describes the prototype detectors we have used and the details of the statistical analysis on which our results are based. We also include a description of our treatment of energy and angular smearing and our choices of the number of bins for each of these variables. Section 4 is devoted to a description of our numerical procedure on the χ^2 sensitivity to the hierarchy. Section 5 summarizes our results and conclusions.

2 Earth-matter effects in atmospheric neutrino oscillation probabilities

In calculating atmospheric electron and muon event rates, the neutrino oscillation probabilities corresponding to the disappearance channels $P_{\mu\mu}$ and P_{ee} and appearance channels $P_{\mu e}$ and

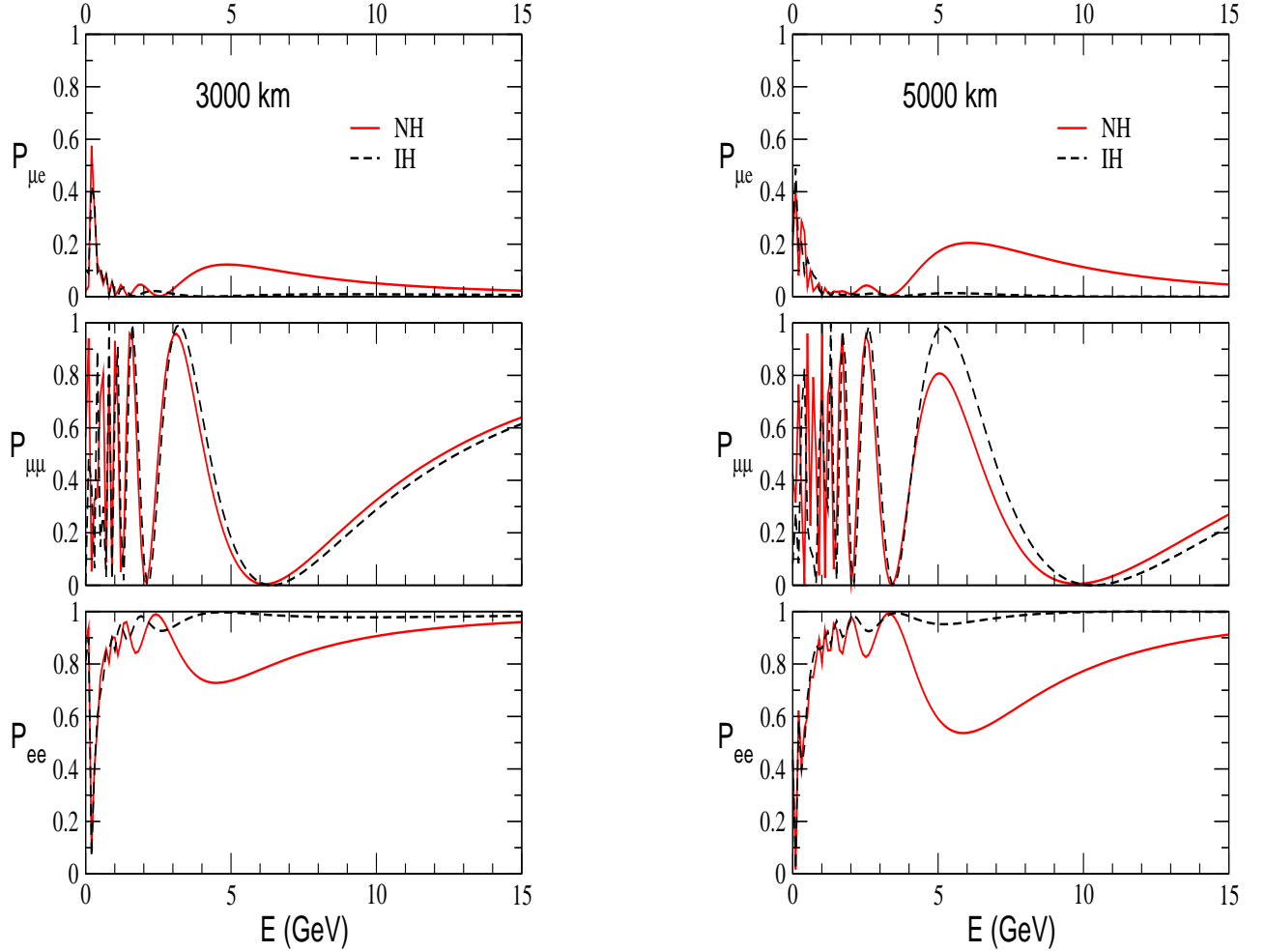


Figure 1: The probabilities $P_{\mu e}$, $P_{\mu\mu}$ and P_{ee} in matter plotted versus neutrino energy for two baselines, 3000 km (left panel) and 5000 km (right panel). The solid curves correspond to NH ($\Delta m_{31}^2 > 0$), while the dashed curves are for IH ($\Delta m_{31}^2 < 0$). Here, we use the neutrino parameter values listed in Eq. 1.

$P_{e\mu}$ are of direct relevance³. For the long path-lengths under consideration here, we need to explicitly take into account the varying density profile of the earth, and for this purpose we use the Preliminary Reference Earth Model (PREM) [46]. In Figures 1 and 2, we plot the three probabilities $P_{\mu e}$, $P_{\mu\mu}$ and P_{ee} as a function of energy for both normal and inverted hierarchies for four different path-lengths in the range 3000–10000 km. These curves result from numerically solving the full three flavour neutrino propagation equation through the earth. In obtaining them we have used the following values for neutrino parameters:

$$\begin{aligned}
 |\Delta m_{31}^2| &= 2.5 \times 10^{-3} \text{ eV}^2, & \Delta m_{21}^2 &= 8.0 \times 10^{-5} \text{ eV}^2, \\
 \sin^2 \theta_{12} &= 0.31, & \sin^2 2\theta_{23} &= 1.0, & \sin^2 2\theta_{13} &= 0.1
 \end{aligned}
 \tag{1}$$

Figures 1 and 2 demonstrate the following qualitative features :

³ $P_{\alpha\beta}$ denotes the probability for transition from $\nu_\alpha \rightarrow \nu_\beta$.

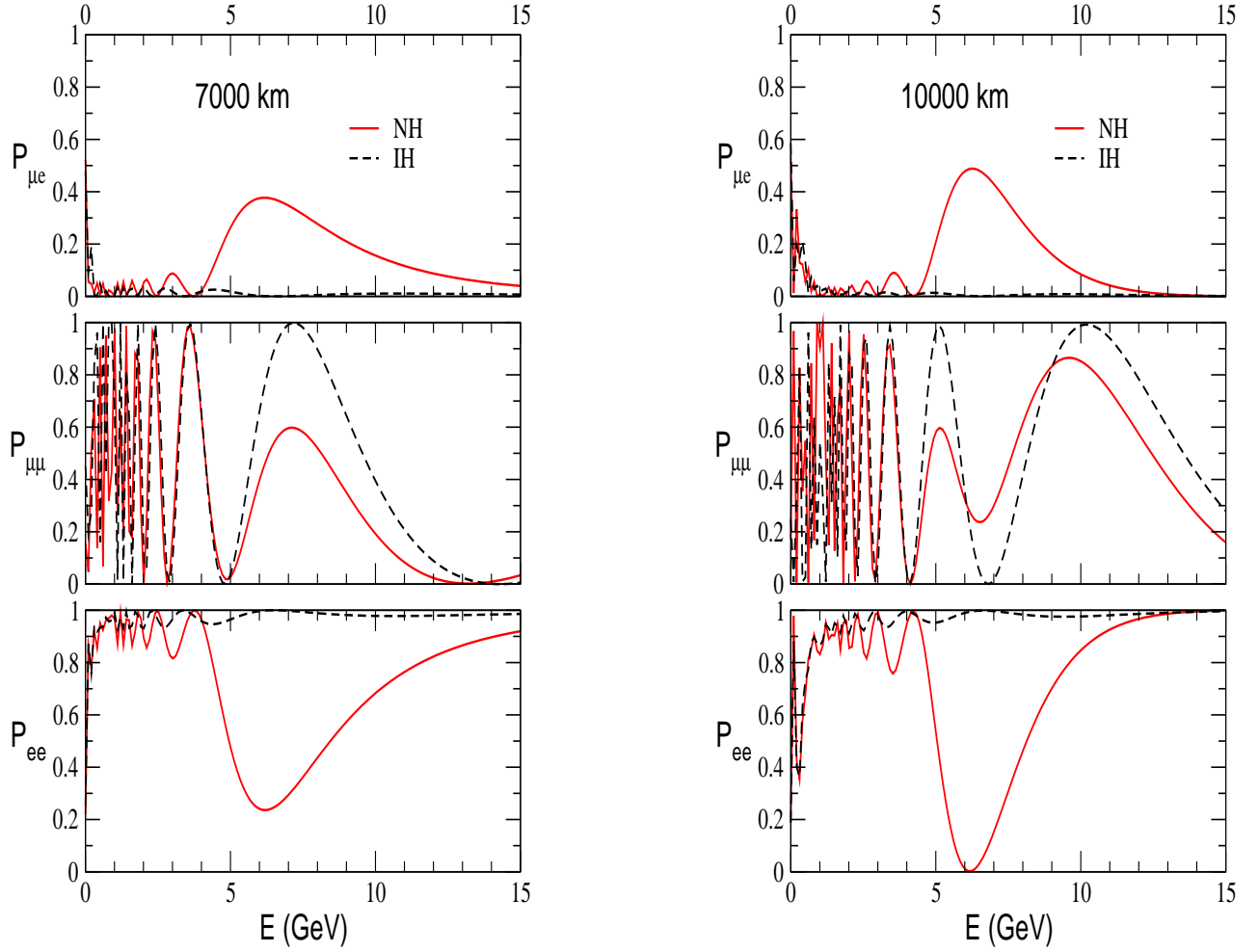


Figure 2: The probabilities $P_{\mu e}$, $P_{\mu\mu}$ and P_{ee} in matter plotted versus neutrino energy for two baselines, 7000 km (left panel) and 10000 km (right panel). The solid curves correspond to NH ($\Delta m_{31}^2 > 0$), while the dashed curves are for IH ($\Delta m_{31}^2 < 0$). Here, we use the neutrino parameter values listed in Eq. 1.

- The differences between the probability values for the two types of hierarchy in all the channels are maximized in the energy range 4–10 GeV.
- Matter effects in $P_{\mu e}$ in case of a NH manifest themselves by a *rise* over the corresponding value for an IH over the range of energies and baselines considered in these figures.
- On the other hand, matter effects in $P_{\mu\mu}$ for a NH manifest themselves as a *decrease* over the IH value in certain energy and baseline ranges and an *increase* in others (*e.g.* for baselines around 10000 km).
- The value of P_{ee} for a NH consistently shows a *fall* compared to the value with an IH for all four baselines in the energy range 2–10 GeV. This fall can be as high as 100% (*e.g.* for baselines around 10000 km).

We discuss these features below, using the one mass scale dominant (OMSD) approximation, which amounts to neglecting the smaller mass-squared difference Δm_{21}^2 in comparison to Δm_{31}^2 . The condition for this approximation to be valid is

$$\frac{\Delta m_{21}^2 L}{E} \ll 1 \quad (2)$$

Alternatively, this corresponds to $L/E \ll 10^4$ km/GeV. For multi-GeV neutrinos, this condition is violated only for a small fraction of events with $E \simeq 1$ GeV and $L \geq 10^4$ km. Hence, effectively Eq. 2 is valid for most of the energies and pathlengths under consideration here. Additionally, the OMSD approximation is not valid for very small θ_{13} , since the terms containing the small parameter Δm_{21}^2 can be dropped only if they are small compared to the leading order terms containing θ_{13} ⁴.

Making this approximation and assuming constant matter density, the probabilities $P_{\mu e}$, P_{ee} and $P_{\mu\mu}$ in matter are given by

$$P_{\mu e}^m = \sin^2 \theta_{23} \sin^2 2\theta_{13}^m \sin^2 \left[1.27 (\Delta m_{31}^2)^m \frac{L}{E} \right] \quad (3)$$

The probability for the time-reversed transition $P_{e\mu}^m$ is same as $P_{\mu e}^m$ with the replacement $\delta_{CP} \rightarrow -\delta_{CP}$ for a symmetric matter density profile like the PREM profile. The OMSD analytical expressions are insensitive to δ_{CP} , hence, $P_{e\mu}^m = P_{\mu e}^m$ in this limit. In general, the two probabilities will be equal only when $\delta_{CP} = 0$.

$$P_{ee}^m = 1 - \sin^2 2\theta_{13}^m \sin^2 \left[1.27 (\Delta m_{31}^2)^m \frac{L}{E} \right] \quad (4)$$

⁴Expressions of probabilities containing corrections of the order of $\Delta m_{21}^2/\Delta m_{31}^2$ can for instance be found in [47–50].

$$\begin{aligned}
P_{\mu\mu}^m &= 1 - \cos^2 \theta_{13}^m \sin^2 2\theta_{23} \sin^2 \left[1.27 \left(\frac{\Delta m_{31}^2 + A + (\Delta m_{31}^2)^m}{2} \right) \frac{L}{E} \right] \\
&\quad - \sin^2 \theta_{13}^m \sin^2 2\theta_{23} \sin^2 \left[1.27 \left(\frac{\Delta m_{31}^2 + A - (\Delta m_{31}^2)^m}{2} \right) \frac{L}{E} \right] \\
&\quad - \sin^4 \theta_{23} \sin^2 2\theta_{13}^m \sin^2 \left[1.27 (\Delta m_{31}^2)^m \frac{L}{E} \right]
\end{aligned} \tag{5}$$

The mass squared difference $(\Delta m_{31}^2)^m$ and mixing angle $\sin^2 2\theta_{13}^m$ in matter are related to their vacuum values by

$$\begin{aligned}
(\Delta m_{31}^2)^m &= \sqrt{(\Delta m_{31}^2 \cos 2\theta_{13} - A)^2 + (\Delta m_{31}^2 \sin 2\theta_{13})^2} \\
\sin 2\theta_{13}^m &= \frac{\Delta m_{31}^2 \sin 2\theta_{13}}{\sqrt{(\Delta m_{31}^2 \cos 2\theta_{13} - A)^2 + (\Delta m_{31}^2 \sin 2\theta_{13})^2}}
\end{aligned} \tag{6}$$

where

$$A = 2 \sqrt{2} G_F n_e E = 2 \times 0.76 \times 10^{-4} \times Y_e \left[\frac{\rho}{\text{g/cc}} \right] \left[\frac{E}{\text{GeV}} \right] \text{eV}^2$$

is the MSW matter potential [51, 52] which depends on the Fermi coupling constant, G_F , the number density of electrons, n_e and energy of the neutrinos, E . Y_e is the fraction of electrons, which is $\simeq 0.5$ for earth matter and ρ is matter density inside earth. The anti-neutrino probabilities can be written down by making the replacement $A \rightarrow -A$ in above equations.

We note that $(\Delta m_{31}^2)^m$ and $\sin 2\theta_{13}^m$ can assume very different values for a NH and an IH, leading to hierarchy dependant differences in all three probabilities given above. Furthermore, large changes in the values of these probabilities arise not just due to the resonance occurring when $\sin^2 2\theta_{13}^m \rightarrow 1$, *i.e.* $A = \Delta m_{31}^2 \cos 2\theta_{13}$, but also due to the matter dependence of the oscillatory L/E terms contained in them. Thus the full effect results from the product of the two types of terms assuming values significantly different from those in vacuum [29, 34, 53].

The matter resonance, which occurs for neutrinos when the hierarchy is normal and for anti-neutrinos when it is inverted, requires

$$E(\text{GeV}) \simeq E_{\text{res}}(\text{GeV}) = \left[\frac{1}{2 \times 0.76 \times 10^{-4} Y_e} \right] \left[\frac{|\Delta m_{31}^2|}{\text{eV}^2} \right] \left[\frac{\text{g/cc}}{\rho} \right] \tag{7}$$

If we use an average density calculated using PREM profile of earth, then we get the resonant energy at various baselines, as listed, in Table 2.

Clearly, hierarchy sensitivity is enhanced when the difference

$$\Delta P_{\alpha\beta} = P_{\alpha\beta}^m(\text{NH}) - P_{\alpha\beta}^m(\text{IH}), \tag{8}$$

L (km)	ρ_{avg} (g/cc)	E_{res} (GeV)
3000	3.32	9.4
5000	3.59	8.7
7000	4.15	7.5
10000	4.76	6.6

Table 2: Values of E_{res} at 13 resonance in case of OMSD are listed as a function of baseline and the average density ρ_{avg} . We have used $|\Delta m_{31}^2| = 2.5 \times 10^{-3} \text{ eV}^2$ and $\sin^2 2\theta_{13} = 0.1$ in Eq. 7.

is large ⁵. It is useful to use the OMSD expressions given above to examine the conditions required for this to occur, and to co-relate them with the large differences between the NH and IH curves visible in Figures 1 and 2 (which, as mentioned earlier, have been obtained using the full three flavour evolution equation and the PREM profile). We proceed to do this below for each of the three probabilities in turn.

2.1 $P_{\mu e}$

From Eq. 3, we can see that this probability reaches its maximum value of $\sin^2 \theta_{23}$ when the resonance condition, $\sin^2 2\theta_{13}^m = 1$ and the condition $\sin^2(1.27(\Delta m_{31}^2)^m L/E) = 1$ are simultaneously satisfied. The second condition yields an energy (henceforth referred to as the **matter peak energy**) given by

$$E_{\text{peak}}^m = \frac{1.27}{(2p+1)\pi/2} (\Delta m_{31}^2)^m L ; p = 0, 1, 2, \dots \quad (9)$$

Thus, the condition for obtaining a maxima in $P_{\mu e}$ can be expressed as $E_{\text{res}} = E_{\text{peak}}^m$. This determines the distance for maximum matter effect via

$$[\rho L]_{\mu e}^{\text{peak}} = 5.18 \times 10^3 \pi \frac{(2p+1)}{\tan 2\theta_{13}} \text{ km g/cc} \quad (10)$$

The above equation is independent of Δm_{31}^2 but depends on the vacuum value of θ_{13} . Note, from the above equation however, that for a given resonant energy, whether or not the oscillatory term in L/E can become maximal in a meaningful way depends on:

- (i) p being low enough and $\sin^2 2\theta_{13}$ large enough that the resultant L is less than the earth's diameter, $L_D = 12742 \text{ km}$. For $\sin^2 2\theta_{13} = 0.1$, the only allowed value of p is p=0, and this gives $L=10200 \text{ km}$ in conjunction with $\rho_{\text{avg}} = 4.8 \text{ g/cc}$.
- (ii) $\sin^2 2\theta_{13}$ not being so small that the OMSD approximation, which we use for the discussion in this section, is invalidated.

⁵Here α, β may be e or μ . $P_{\alpha\beta}^m$ (IH) is computed in each case by reversing the sign of Δm_{31}^2 in the expression for $P_{\alpha\beta}^m$.

For our discussion which follows below leading to Eq. 11 and Eq. 15, the first restriction on $\sin^2 2\theta_{13}$ limits $\sin^2 2\theta_{13} \gtrsim 0.04$ ⁶.

Under these conditions, for a particular value of θ_{13} , one may write,

$$\Delta P_{\mu e}^{\max} = \sin^2 \theta_{23} \left[1 - \frac{\sin^2 2\theta_{13}}{4 - 3 \sin^2 2\theta_{13}} \sin^2 \left[(2p + 1) \frac{\pi}{2} \frac{1}{\sin 2\theta_{13}} \sqrt{4 - 3 \sin^2 2\theta_{13}} \right] \right] \quad (11)$$

Numerically, this reduces to $\Delta P_{\mu e}^{\max} \simeq 0.5$ for $\theta_{23} = \pi/4$ and $\sin^2 2\theta_{13} = 0.1$. Comparing with the top panel of the right-hand set of plots in Figure 2, we see that both the baseline value and $\Delta P_{\mu e}^{\max}$ are in very good agreement with these estimates. For smaller baselines although the resonance condition is achieved the oscillatory term remains < 1 and thus the rise in $P_{\mu e}^m$ in matter for NH is lower. However, since this is an appearance channel even with a moderate increase in probability it is possible to do interesting physics if the backgrounds are well understood.

2.2 P_{ee}

From Eq. 4 it is clear that the condition for obtaining maximum matter effect in P_{ee}^m is the same as that for $P_{e\mu}^m$, *i.e.*, $E_{\text{res}} = E_{\text{peak}}^m$. This gives

$$\Delta P_{ee}^{\max} = \left[-1 + \frac{\sin^2 2\theta_{13}}{4 - 3 \sin^2 2\theta_{13}} \sin^2 \left[(2p + 1) \frac{\pi}{2} \frac{1}{\sin 2\theta_{13}} \sqrt{4 - 3 \sin^2 2\theta_{13}} \right] \right] \quad (12)$$

This quantity is maximized when P_{ee}^m (NH) is at its minimum value of 0 and P_{ee}^m (IH) is at its maximum value, which is close to 1. For $\sin^2 2\theta_{13} = 0.1$. and the earlier baseline value of ≈ 10000 km, this reduces numerically to $\simeq -0.98$, which is manifest in the bottom panel of the right-hand set of curves in Figure 2 [54].

2.3 $P_{\mu\mu}$

The muon disappearance probability is a somewhat more complicated function as can be seen from Eq. 5. In order to understand where and why maximal hierarchy effects arise, we first note from Figures 1 (central right-hand panel) and 2 (central panels in both left-hand and right-hand sets) that large hierarchy sensitivity occurs when the neutrino energy is close to E_{res} (cf Table 2) *and* in the vicinity of a peak or dip in $P_{\mu\mu}^m$ (IH). Since the matter effect in neutrinos is negligible for IH, these curves closely follow the vacuum probability, and in particular have peaks and dips at the same locations.

Noting that the vacuum peak of $P_{\mu\mu}$ occurs when

$$1.27 \frac{\Delta m_{31}^2 L}{E_{\text{peak}}^{\nu}} = p \pi \quad (13)$$

⁶ $\sin^2 2\theta_{13} \gtrsim 0.04$ is obtained by substituting $L = L_D = 12742$ km and $\rho \sim 7$ g/cc. This value is a conservative estimate considering the fact that density at the center of earth is not very well-known and that at such large distances, the constant density approximation is not very good.

and, setting $E_{\text{peak}}^{\text{v}} = E_{\text{res}}$, we obtain

$$[\rho L]_{\mu\mu}^{\text{peak}} \simeq p \pi \times 10^4 \times \cos 2\theta_{13} \text{ km g/cc} \quad (14)$$

For $p=1$, *i.e.*, when the resonance is near the first vacuum peak this leads to $L \simeq 7000$ km (taking the average density to be 4.15 g/cc), which is borne out by the middle panel of the left column of Figure 2. The magnitude of this fall can be estimated by ⁷

$$\begin{aligned} \Delta P_{\mu\mu}^{\text{max,peak}} &\simeq \left[-\sin^2 \left[p \frac{\pi}{2} \sin 2\theta_{13} \right] - \frac{1}{4} \sin^2 \left[p \pi \sin 2\theta_{13} \right] \right. \\ &+ \sin^2 \left[p \frac{\pi}{2} \sqrt{4 - 3 \sin^2 2\theta_{13}} \right] \\ &\left. + \frac{1}{4} \frac{\sin^2 2\theta_{13}}{4 - 3 \sin^2 2\theta_{13}} \sin^2 \left[p \pi \sqrt{4 - 3 \sin^2 2\theta_{13}} \right] \right] \quad (15) \end{aligned}$$

Numerically, this gives a drop in $P_{\mu\mu}^{\text{m}}$ (NH) relative to $P_{\mu\mu}^{\text{m}}$ (IH) of $\simeq -0.4$, which is borne out by central panel in Figure 2 near the region of peak in IH curve.

The right column of Figure 2 also shows that at 10000 km there is a *rise* in $P_{\mu\mu}$ (NH) relative to $P_{\mu\mu}$ (IH) near a dip in the IH probability at ~ 6 GeV. The condition for dip in $P_{\mu\mu}$ in vacuum is

$$1.27 \frac{\Delta m_{31}^2 L}{E_{\text{dip}}^{\text{v}}} = (2p + 1) \frac{\pi}{2} \quad (16)$$

This gives the position of the second vacuum dip (*i.e.* when $p = 1$) for $L = 10000$ km to be around ~ 6.7 GeV. Table 2 shows that at 10000 km the resonance energy is ~ 6.6 GeV. Thus, we have the condition $E_{\text{res}} \approx E_{\text{dip}}^{\text{v}}$ satisfied here for $p=1$. Using this, one can similarly estimate the magnitude of the corresponding rise, and find it to be in good agreement with the figure, *i.e.* about 22% for $p = 1$ ⁸.

It is interesting to note from Eq. 11 and from Figure 2 that at this baseline there is a 50% rise in $P_{\mu e}$ probability over IH. Since $\Delta P_{\mu\tau} = -(\Delta P_{\mu e} + \Delta P_{\mu\mu})$ this implies a 70% matter induced decrease in the $P_{\mu\tau}$ probability, which is a transition probability between two species of neutrinos for which matter effect occurs only via neutral current interactions and is identical to both. This dramatic matter driven decrease is a genuine three flavour effect and was first pointed out in [55].

To summarize, we have discussed the important features of 3 generation oscillation probabilities in matter corresponding to appearance and disappearance channels. In order to do that, we have (in this section only) worked in the OMSD approximation, which allows the use of tractable analytic expressions. We have emphasized those features which percolate into the disappearance probability for electron and muon events and modify the expected atmospheric

⁷In order to simplify this expression, we have set $\cos^2 2\theta_{13} = 1$.

⁸For $p = 0$, the value of $\Delta P_{\mu\mu}$ is small since matter effects are not appreciable at the associated baseline of 5000 km.

neutrino signal in water Čerenkov and magnetized iron detectors in a hierarchy dependent manner, and examined the cases where these effects are maximized. However, the full effects are spread over a wide band of energies and baselines (4–12 GeV and 3000–12000 km⁹ respectively). In spite of the fact that the effects vary in significance over these ranges for each of the probabilities, cumulatively they provide a powerful discriminator of the hierarchy. We exploit this fact by doing a bin-by-bin χ^2 analysis of simulated data to determine the potential for hierarchy determination.

3 Detector Characteristics

In this section we describe the details of the two types of detectors that we have considered for our study.

3.1 Water Čerenkov Detectors

We consider a prototype megaton Water Čerenkov detector based on the proposed Hyper-Kamiokande (HK) detector. HK will essentially be a scaled up version of the Super-Kamiokande (SK) detector with the total volume increased to 1 Mt and a fiducial volume of 545 Kt. R&D initiatives are in progress currently to study the non-trivial physics and engineering issues which arise due to this scaling up in size [59].

Since water Čerenkov detectors can discriminate between muon and electron events, the full atmospheric neutrino spectrum can be studied. They are, however, insensitive to lepton charge, thus neutrino and anti-neutrino events must be added together. In the following, we add the events of ν_μ , whose charged current (CC) interactions produce a μ^- , and those of $\bar{\nu}_\mu$, whose CC interactions produce a μ^+ , and call the sum to be muon events. Similarly, we add the CC events of ν_e and $\bar{\nu}_e$ and call the sum to be electron events.

In this case the hierarchy sensitivity is determined by the difference in the total number of events. For instance for muon events this quantity is

$$\Delta N = (N_{\mu^-}^{\text{NH}} + N_{\mu^+}^{\text{NH}}) - (N_{\mu^-}^{\text{IH}} + N_{\mu^+}^{\text{IH}}) = (N_{\mu^-}^{\text{NH}} - N_{\mu^-}^{\text{IH}}) + (N_{\mu^+}^{\text{NH}} - N_{\mu^+}^{\text{IH}}) = \Delta N_{\mu^-} + \Delta N_{\mu^+} \quad (17)$$

If the hierarchy is normal, matter effects induce large changes in neutrino appearance and disappearance probabilities and hence in $N_{\mu^-}^{\text{NH}}$, while leaving anti-neutrino probabilities and hence $N_{\mu^+}^{\text{NH}}$ essentially the same as the vacuum probabilities. If the hierarchy is inverted, then anti-neutrino probabilities undergo large changes and neutrino probabilities remain the same. Thus ΔN_{μ^-} and ΔN_{μ^+} have opposite signs leading to cancellations. But ΔN_{μ^-} is larger by a factor 2.5–3 because the neutrino-nucleon cross sections are higher by this factor and hence the cancellation is only partial. A similar reasoning holds for electron events. This leads to hierarchy sensitivity in water Čerenkov detectors. It is not as good as that of detectors with

⁹Beyond 10500 km, the neutrinos start traversing the core, causing the onset of mantle-core interference effects [36, 56–58]. Our full numerical calculations incorporate the difference between NH and IH probabilities due to these effects.

charge discrimination capability but the proposed megaton mass overrides this disadvantage and provides the statistics necessary for a determination of the hierarchy.

Since no simulation studies for atmospheric neutrinos are available for **HK** we assume the same detector characteristics as in the **SK** detector but with increased statistics. Our results are for an exposure of 1.8 Mt yr, which corresponds to 3.3 years of running time. In our calculation, we have put in a lepton energy threshold of 1 GeV, since Δm_{31}^2 driven matter effects arise in this energy range and the determination of $\text{sign}(\Delta m_{31}^2)$ is better achieved with higher energy neutrinos. This leads to a threshold correction in the cross section [38], which we incorporate into our calculations. We use the detection efficiencies of the **SK** experiment [60,61] for multi-GeV one-ring muon (both fully and partially contained μ -like) events and electron (e-like) events. The L/E analysis of **SK** muon-data has demonstrated the feasibility of reconstructing the neutrino energy in a water Čerenkov detector from Monte Carlo simulation by fitting it to the total energy of the charged particles [61]. Similarly the direction of the neutrino can also be determined from the reconstructed direction of the muon [62]. For fully contained (FC) (partially contained (PC)) multi-GeV muon events the energy smearing is 17% (24%) while the angular smearing is $17^\circ(10^\circ)$. In our calculations for purposes of comparison with magnetized iron calorimeter detectors, we use an overall 15% energy smearing and 10° angular smearing for both types of events. While this is somewhat optimistic, we will discuss in detail the extent to which the sensitivity to hierarchy depends on smearing.

Both muon and electron events in this detector have contributions coming from background processes. The backgrounds in the FC events are due to cosmic ray muons, PMT flashes and neutron events from the rock surrounding the detector [63]. For PC events the cosmic ray muons constitute the main background. These backgrounds can, however, largely be eliminated during the data reduction procedure [63]. The remaining backgrounds occur due to (a) neutral current (NC) events and (b) ν_μ (ν_e) induced CC events for electron (muon) data sample. The expected backgrounds in the case of atmospheric neutrino interactions are estimated by the **SK** Monte Carlo and are given in [63]. For multi-GeV one-ring muon events the contamination due to above processes is estimated to be about 0.3% whereas for multi-GeV one-ring electron events have a background of about 10% from NC events and about 7% from ν_μ induced CC events.

3.2 Magnetized Iron Detectors

We consider a prototype magnetized iron detector along the lines of the India-based Neutrino Observatory [6] (**INO**). This detector is expected to have a modular structure with an initial running mass of 50 kT, building up to a final mass of 100 kT. It will consist of 140 layers of iron plates about 6 cm thick, with gaps of about 2.5 cm between them housing the active elements. These have been chosen to be RPC's (Resistive Plate Chambers), made of glass or bakelite and containing a mixture of gases. The (50 kT) structure is divided into three modules, with an overall lateral size of 48×16 meters and a height of 12 meters. A magnetic field of about 1.3 Tesla will provide charge discrimination capability to the detector. We consider an exposure of 1.0 Mt yr, which corresponds to 10 years of running time.

The high density of iron renders this detector insensitive to sub-GeV muons and electrons

of any energy. In our calculations, we have assumed a detection threshold of 1 GeV for muons and included the corresponding threshold correction in the cross section. An overall detection efficiency of 87% and a charge identification efficiency of 100% is assumed¹⁰. The magnetic field allows charge identification and thus the interactions of ν_μ and $\bar{\nu}_\mu$ can be studied separately. Thus ΔN_{μ^-} and ΔN_{μ^+} defined in Eq. 17 can each be determined. The hierarchy sensitivity in this case depends on the sum of the magnitudes of these quantities. Therefore the partial cancellation occurring for water Čerenkov detectors does not take place for charge discriminating detectors giving them an advantage over the former.

The energy and the direction of the neutrino in INO can be reconstructed from the muon track [6]. The energy of the neutrino is the sum total of the energy of the muon and the hadrons. The latter is difficult to reconstruct for individual hadrons. However, one may use the hit multiplicity of charged particles distinct from the muon track to calibrate the total energy of the hadrons in the event. It is reasonable to assume energy smearing of 15% and angular smearing of 10° for this detector, which are the values we adopt in our numerical work. As in the case of the water Čerenkov detector, we study the sensitivity of this detector's capability for hierarchy determination in case its resolutions are different from those assumed by us.

Finally, we comment on the background signal in this detector. A preliminary study using a GEANT based simulation of cosmic ray muon background in INO shows that these are unlikely to mimic the signal [37]. Other backgrounds can originate due to NC interactions, such as $\nu_x + d(u) \rightarrow \nu_x + d(u) (+ q \bar{q})$, where the quarks in the final state can produce mesons along with other hadrons. The decay of these mesons produces secondary muons which can contaminate the signal. However, simulations have shown that the 6 cm thickness of the iron plates is sufficient to absorb any pions and kaons in the 1–10 GeV range before they can decay. In addition, the oscillated ν_τ s can produce τ which can decay to muons with a branching ratio of 17.36% via $\nu_\tau \rightarrow \mu^- + \bar{\nu}_\mu + \nu_\tau$. However the number of these secondary muons are expected to be small because of the higher τ production threshold of 3.5 GeV. Also these muons are softer in energy and hence can be eliminated by suitable energy cuts [64].

In Table 3, the comparative characteristics of the two detectors HK and INO are listed.

4 Numerical Procedure

The total number of CC events is obtained by folding the relevant incident neutrino fluxes with the appropriate disappearance and appearance probabilities, relevant CC cross sections, the efficiency for muon detection, the detector resolution, mass and the exposure time. The total CC cross section used here is the sum of quasi-elastic, single meson production and deep inelastic cross sections. The cross sections for the water Čerenkov detector are taken from [63] and for the magnetized iron detector are taken from [65–67]. For the incident atmospheric neutrino fluxes we use the tables from [68] where a 3-dimensional model is employed for flux

¹⁰This charge identification efficiency is valid for neutrino energy $\ll 1$ TeV.

Property	HK	INO
Detector Technology	Water Čerenkov	Iron calorimeter
Fiducial Volume	545 Kt	100 Kt
Exposure Time	3.3 yr	10 yr
Energy Threshold	1 GeV	1 GeV
Energy smearing	15%	15%
Angular Smearing	10°	10°
Detection Efficiency	E-dependent	87%
Charge Discrimination	No	Yes
Muon Events	Yes	Yes
Electron Events	Yes	No

Table 3: Properties of the two detectors considered in our analysis, HK and INO.

calculation ¹¹.

For our analysis, we look at the neutrino energy range of 2–10 GeV and the cosine of the zenith angle (θ) range of -1.0 to -0.1. These are divided into bins, and the μ^- event rate in a specific energy bin with width dE and the solid angle bin with width $d\Omega$ is expressed as :

$$\frac{d^2N_\mu}{d\Omega dE} = \frac{1}{2\pi} \left[\left(\frac{d^2\Phi_\mu}{d \cos \theta dE} \right) P_{\mu\mu} + \left(\frac{d^2\Phi_e}{d \cos \theta dE} \right) P_{e\mu} \right] \sigma_{CC} D_{\text{eff}} \quad (18)$$

Here $\Phi_{\mu,e}$ are the atmospheric fluxes (ν_μ and ν_e), σ_{CC} is the total CC cross section and D_{eff} is the detector efficiency. The μ^+ event rate is similar to the above expression with the fluxes, probabilities and cross sections replaced by those for anti-muons. Similarly, the e^- event rate in a specific energy and zenith angle bin is expressed as follows:

$$\frac{d^2N_e}{d\Omega dE} = \frac{1}{2\pi} \left[\left(\frac{d^2\Phi_\mu}{d \cos \theta dE} \right) P_{\mu e} + \left(\frac{d^2\Phi_e}{d \cos \theta dE} \right) P_{ee} \right] \sigma_{CC} D_{\text{eff}} \quad (19)$$

with the e^+ event rate being expressed in terms of anti-neutrino fluxes, probabilities and cross sections.

For the HK analysis, the sum of $\mu^-(e^-)$ events and $\mu^+(e^+)$ events is taken to compute the total muon (electron) event rate, since the detector is insensitive to lepton charge. For the INO analysis, however, the μ^- and μ^+ event rates are separately used given its charge identification capability.

¹¹The INO facility is expected to be housed at Pushep (lat: North 11.5°, long: East 76.6°). The Honda fluxes in [68] are calculated for SK (lat: North 36.4°, long: East 137.3°). However, because of unavailability of the fluxes at the specific INO latitude we use the Honda fluxes given at the SK site for INO .

4.1 Energy and angular smearing:

We take into account the smearing in both energy and zenith angle, assuming a Gaussian form of resolution function, R . For energy, we use

$$R(E_t, E_m) = \frac{1}{\sqrt{2\pi}\sigma} \exp\left[-\frac{(E_m - E_t)^2}{2\sigma^2}\right] \quad (20)$$

Here, E_m and E_t denote the measured and true values of energy respectively. The smearing width σ is a fraction of E_t . Most of our calculations are performed assuming this fraction to be 15%. We also calculate how our results vary if this resolution fraction is reduced to 10% or 5%.

The smearing function for the zenith angle is a bit more complicated because the direction of incident neutrino is specified by two variables: the polar angle θ_t and the azimuthal angle ϕ_t . We denote both these angles together by Ω_t . The measured direction of the neutrino, with polar angle θ_m and azimuthal angle ϕ_m , which together we denote by Ω_m , is expected to be within a cone of half angle $\Delta\theta$ of the true direction. Since the angular smearing is to be done in a cone around the direction specified by (θ_t, ϕ_t) , we cannot assume the smearing function to be a function of the polar angle only. If we consider a small cone whose axis is given by the direction θ_t, ϕ_t , then the set of directions within the cone have different polar angles and azimuthal angles. Therefore, we need to construct a smearing function which takes into account the change in the azimuthal coordinates as well. Such an angular smearing function is given by

$$R(\Omega_t, \Omega_m) = N \exp\left[-\frac{(\theta_t - \theta_m)^2 + \sin^2\theta_t (\phi_t - \phi_m)^2}{2(\Delta\theta)^2}\right] \quad (21)$$

Details of the computation of the normalization constant N appearing in the above equation are given in the Appendix A.

The event rate with the smearing factors taken into account is given by

$$\frac{d^2N_\mu}{d\Omega_m dE_m} = \frac{1}{2\pi} \int_1^{100} dE_t \int d\Omega_t R(E_t, E_m) R(\Omega_t, \Omega_m) [\Phi_\mu^d P_{\mu\mu} + \Phi_e^d P_{e\mu}] \sigma_{CC} D_{\text{eff}} \quad (22)$$

where we have denoted $(d^2\Phi/d\cos\theta dE)_\mu \equiv \Phi_\mu^d$ etc.. Strictly speaking, the range of integration for the true energy of the neutrino E_t should be from 0 to ∞ . However, given the fact that we set a lower threshold of 1 GeV for the lepton energy, our choice of the lower limit of integration is dictated by the requirement that the neutrino be more energetic than the lepton. Taking an upper limit of 100 GeV for the true energy is justified because the probability of spillover of events from bins above 100 GeV to bins below 10 GeV due to smearing is insignificant, and the number of events above 100 GeV is quite small due to the steeply falling neutrino flux.

In Figure 3, we show the effect of angular smearing on distribution of muon events in HK assuming a NH. The figure also shows the $\cos\theta_m$ distribution for the two special cases of *no* smearing *without* and *with* oscillations. It demonstrates the washing out of oscillatory behaviour in the event distribution as the angular smearing width is increased. Note that the distribution with oscillation and without smearing shows some distortion in its shape

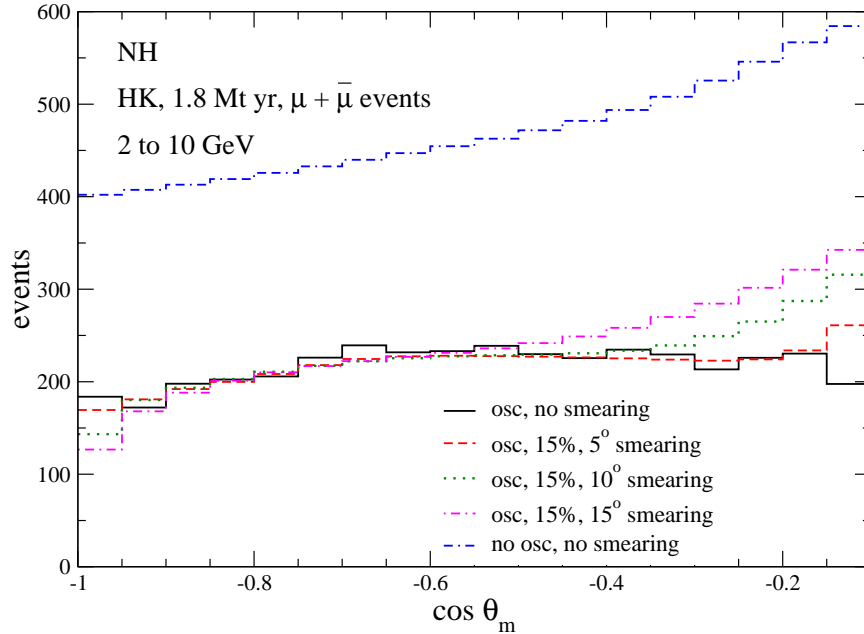


Figure 3: The muon event rate for HK (1.8 Mt yr) with different values of angular smearing and 15% energy smearing, as well as without smearing with and without oscillations, plotted versus $\cos \theta_m$ taking 18 bins in the range -1.0 to -0.1. The energy range taken is 2 to 10 GeV, and the hierarchy is taken to be normal.

compared to the distribution without oscillation. When the angular smearing is introduced, this oscillatory distortion is washed out progressively as the value of smearing is increased. For smearing with a large angular resolution of 15° , the distribution with oscillations resembles the unoscillated distribution in its shape.

Figure 4 shows the muon event distribution in HK for NH and IH for six energy bins of width 1 GeV each in the energy range of 4–10 GeV. From these figures it is clear that below the resonant energy, the difference between the normal and inverted hierarchy distributions is negligible (note that $E_{\text{res}} > 6$ GeV for all baselines considered here, as described in Table 2). Around resonance, *i.e.* from the 6–7 GeV energy bin, the difference begins to be significant. A little above the resonance, the event numbers fall off, but a reasonable difference between NH and IH distributions persists, which contributes significantly to the hierarchy sensitivity.

χ^2 analysis

We study the χ^2 sensitivity to the mass hierarchy for various different values of energy and angular resolution. For HK, we use a binned distribution of muon as well as electron events in various E_m and $\cos \theta_m$ bins. For INO, we use similar binning for μ^- and μ^+ events.

From Figure 4 we note that each bin contains ≥ 5 events. Hence Gaussian error analysis may be used. In the limit when only statistical errors are taken into account, the standard

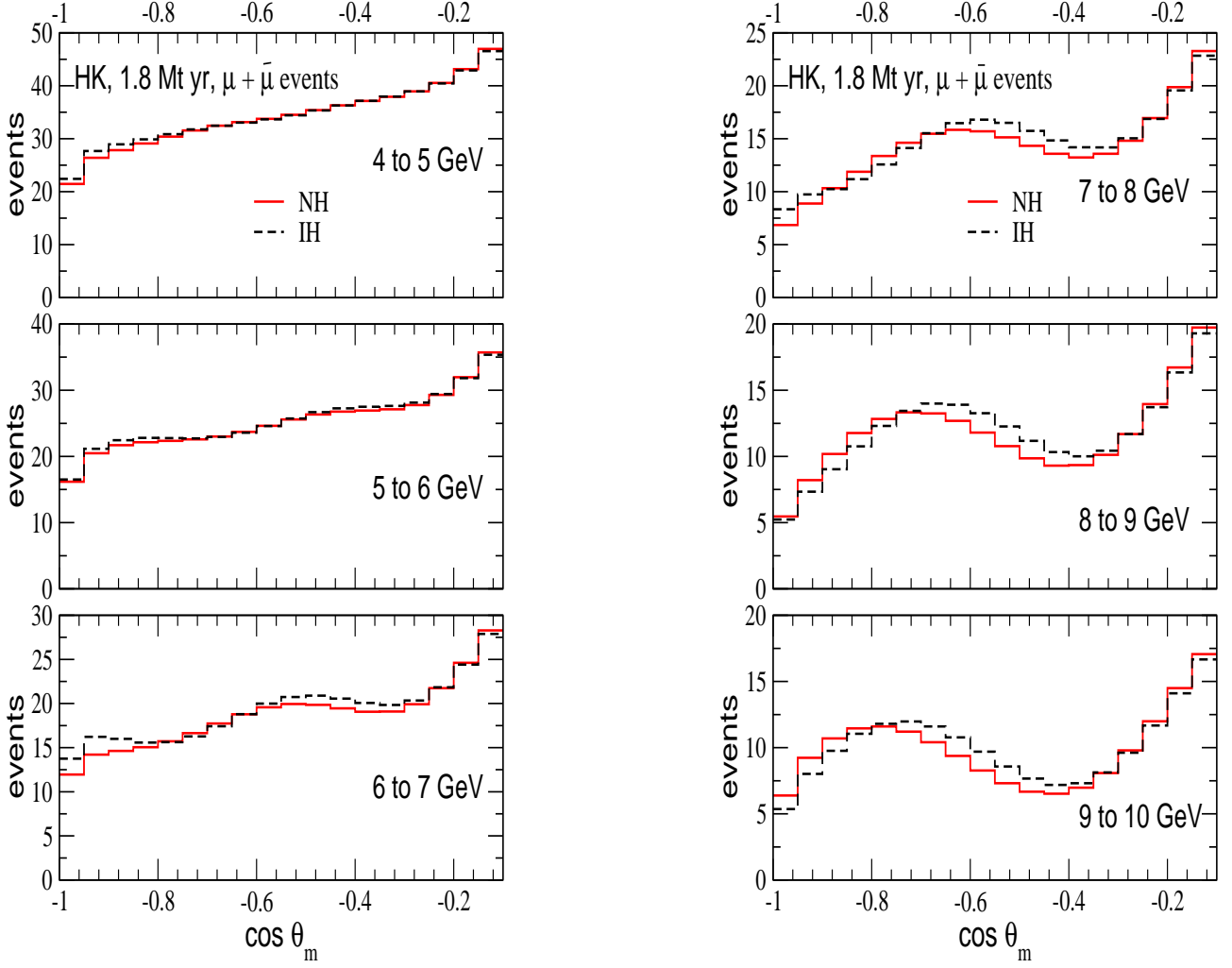


Figure 4: The muon event rate for HK (1.8 Mt yr) with 10° angular smearing and 15% energy smearing plotted versus $\cos \theta_m$ taking 18 bins in the range -1.0 to -0.1, for 6 different energy bins in the range 4 to 10 GeV, for both normal and inverted hierarchy.

Gaussian definition of binned χ^2 is:

$$\chi_{\text{stat}}^2 = \sum_{i=E_m \text{ bins}} \sum_{j=\cos \theta_m \text{ bins}} \frac{[N_{ij}^{\text{ex}} - N_{ij}^{\text{th}}]^2}{N_{ij}^{\text{ex}}} \quad (23)$$

Here, N_{ij}^{ex} is the experimental and N_{ij}^{th} is theoretical number of events in the ij^{th} bin.

However, in addition to the statistical uncertainties, one also needs to take into account various theoretical and systematic uncertainties. In our analysis we include the uncertainties coming from

- A flux normalization error of 20%,
- A tilt factor [69] which takes into account the deviation of the atmospheric fluxes from a power law,

- A zenith angle dependence uncertainty of 5%,
- An overall cross section uncertainty of 10%,
- An overall systematic uncertainty of 5%.

These uncertainties are included using the method of pulls described in [69–71]. This method allows us to take into account the various uncertainties in theoretical inputs and experimental systematics in a simple, straight-forward way.

In this method, the uncertainty in fluxes and cross sections and the systematic uncertainties are taken into account by allowing these inputs to deviate from their standard values in the computation of N_{ij}^{th} . Let the k^{th} input deviate from its standard value by $\sigma_k \xi_k$, where σ_k is its uncertainty. Then the value of N_{ij}^{th} with the changed inputs is given by

$$N_{ij}^{\text{th}} = N_{ij}^{\text{th}}(\text{std}) + \sum_{k=1}^{\text{npull}} c_{ij}^k \xi_k \quad (24)$$

where $N_{ij}^{\text{th}}(\text{std})$ is the theoretical rate for bin ij , calculated with the standard values of the inputs and npull is the number of sources of uncertainty, which in our case is 5. The ξ_k 's are called the ‘‘pull’’ variables and they determine the number of σ 's by which the k^{th} input deviates from its standard value. In Eq. 24, c_{ij}^k is the change in N_{ij}^{th} when the k^{th} input is changed by σ_k (*i.e.* by 1 standard deviation). The uncertainties in the inputs are not very large. Therefore, in Eq. 24 we only considered the changes in N_{ij}^{th} which are linear in ξ_k . Thus we have a modified χ^2 defined by

$$\chi^2(\xi_k) = \sum_{ij} \frac{\left[N_{ij}^{\text{th}}(\text{std}) + \sum_{k=1}^{\text{npull}} c_{ij}^k \xi_k - N_{ij}^{\text{ex}} \right]^2}{N_{ij}^{\text{ex}}} + \sum_{k=1}^{\text{npull}} \xi_k^2 \quad (25)$$

where the additional term ξ_k^2 is the penalty imposed for moving k^{th} input away from its standard value by $\sigma_k \xi_k$. The χ^2 with pulls, which includes the effects of all theoretical and systematic uncertainties, is obtained by minimizing $\chi^2(\xi_k)$, given in Eq. 25, with respect to all the pulls ξ_k :

$$\chi_{\text{pull}}^2 = \text{Min}_{\xi_k} \left[\chi^2(\xi_k) \right] \quad (26)$$

4.2 Optimization of number of bins

We do binning in the measured energy E_m and the cosine of the measured zenith angle (which is the measured polar angle of the incident neutrino) $\cos\theta_m$. For optimization purposes, we compute the χ^2 with pull for various different choices of the number of energy and zenith angle bins. We found that the sensitivity for muon events improves with an increase in the number of bins, and is optimal for about 15 $\cos\theta_m$ bins and 15 energy bins. For the electron events, the optimization occurs for a lower number of bins. This difference can be understood from the behaviour of P_{ee} , $P_{\mu e}$ and $P_{\mu\mu}$ in Figures 1 and 2. In the resonance energy range of 4–6 GeV, oscillation probabilities involving ν_e are relatively less sharply oscillating, whereas

the $P_{\mu\mu}$ oscillates rapidly. Thus a finer binning in energy is needed for muon events to capture these oscillations, whereas a much coarser energy binning is enough to capture the change due to matter effect in electron events. However, because the energy resolution for a water Čerenkov detector gets poorer at higher energies in the GeV range, a very fine binning in energy for $E_m > 2$ GeV is not realistic. Hence we consider a bin division into 8 E_m bins in the range 2–10 GeV and 18 $\cos\theta_m$ bins in the range -1.0 to -0.1. The results given in the subsequent sections are with this binning.

4.3 Marginalization over Neutrino Parameters

In order to determine the optimum number of bins we have used the χ^2_{pull} from Eq. 26 where only the uncertainties in inputs such as fluxes and cross sections are taken into account, holding the values of the oscillation parameters fixed in the calculation of both N_{ij}^{ex} and N_{ij}^{th} . However, in general, the values of the mass-squared differences $|\Delta m_{31}^2|$ and Δm_{21}^2 and the mixing angles θ_{12} , θ_{23} and θ_{13} can vary over a range that reflects the uncertainty in our knowledge. Holding their values as fixed in computing both N_{ij}^{ex} and N_{ij}^{th} is tantamount to assuming that they are known to infinite precision, which is not realistic. To take into account the uncertainties in these parameters, we define the **marginalized** χ^2 for hierarchy sensitivity as,

$$\chi_{\text{min}}^2 = \text{Min} \left[\chi^2(\xi_k) + \left(\frac{|\Delta m_{31}^2|^{\text{true}} - |\Delta m_{31}^2|}{\sigma(|\Delta m_{31}^2|)} \right)^2 + \left(\frac{\sin^2 2\theta_{23}^{\text{true}} - \sin^2 2\theta_{23}}{\sigma(\sin^2 2\theta_{23})} \right)^2 + \left(\frac{\sin^2 2\theta_{13}^{\text{true}} - \sin^2 2\theta_{13}}{\sigma(\sin^2 2\theta_{13})} \right)^2 \right] \quad (27)$$

$\chi^2(\xi_k)$ in the above equation, is computed according to the definition given in Eq. 25.

We use the following procedure for our analysis.

- We simulate the number of events in 8 bins in the measured energy E_m and 18 bins in the measured zenith angle $\cos\theta_m$ for a set of “true values” for the six neutrino parameters – $|\Delta m_{31}^2|$, θ_{23} , θ_{13} , Δm_{21}^2 , θ_{12} and δ_{CP} and for a “true hierarchy”. This is our “experimental data” – N_{ij}^{ex} .
- In the case of Δm_{21}^2 , θ_{12} , $|\Delta m_{31}^2|$ and θ_{23} , the *true values* are the current best-fit values. The true value of δ_{CP} is assumed to be zero in our analysis ¹².
- Matter effects, which are crucial for making a distinction between the hierarchies, are proportional to $\sin^2 2\theta_{13}$. At present there is only an upper limit on $\sin^2 2\theta_{13}$ (< 0.15). Therefore, we compute the χ^2 for various different “true” input values of this parameter in its permissible range.

¹²The oscillation probabilities have only a weak dependence on δ_{CP} for values of $\sin^2 2\theta_{13}$ which will be measurable in the forthcoming reactor neutrino experiments (≥ 0.05). In the next section, we will explicitly show that for both water Čerenkov and magnetized iron detectors, χ^2 has only a weak dependence on δ_{CP} . Therefore we set $\delta_{\text{CP}} = 0$.

- In order to test at what statistical significance the “wrong hierarchy” can be disfavoured, we calculate the theoretical expectation in each bin – N_{ij}^{th} assuming the “wrong hierarchy”.
- During this calculation of theoretical event rates we fix the solar parameters Δm_{21}^2 and θ_{12} at their best-fit values. Since the solar parameters have only marginal effect on the probabilities for the energies and pathlengths relevant for us, our results will not change significantly if these two parameters are allowed to vary in their currently allowed range. For the same reason we keep the CP phase δ_{CP} fixed at its true value which we have taken as zero in this calculation.
- However, we allow the parameters $\sin^2 2\theta_{13}$, $\sin^2 2\theta_{23}$ and $|\Delta m_{31}^2|$ to vary within the following ranges :

1. $|\Delta m_{31}^2|$ is allowed to vary in the range $2.35 \times 10^{-3} - 2.65 \times 10^{-3} \text{ eV}^2$.
2. $\sin^2 2\theta_{23}$ is varied between 0.95 and 1.0. However, $P_{\mu e}$ and $P_{\mu\mu}$ in matter are dependent on $\sin^2 \theta_{23}$. For $\sin^2 2\theta_{23} < 1$ there exist two allowed values of θ_{23} (the so called octant ambiguity). In our calculation we consider both values. Hence we consider a range $0.4 < \sin^2 \theta_{23} < 0.6$.
3. $\sin^2 2\theta_{13}(\text{true})$ is varied from 0.0 to 0.15. The current 3σ bound is $\sin^2 2\theta_{13} < 0.15$ [1].

- In computing χ_{min}^2 , we have added the *priors* for the neutrino parameters which puts a penalty for moving away from the true value. Shifting further from the *true value* of a parameter, would worsen the fit of the experiment which measured that parameter. By adding the *priors* we are effectively minimizing χ^2 of *our data* together with those of the experiments measuring the neutrino parameters. The results, obviously, depend on the choice of true parameter values.

In the expression for χ_{min}^2 , the prior for the mixing angle θ_{23} is given in terms of $\sin^2 2\theta_{23}$. This is valid because the quantity which will be measured in future ν_μ disappearance experiments is $\sin^2 2\theta_{23}$ and the priors are added to take into account the fit to the data which made the measurements.

In Eq. 27, σ denotes 1σ errors. We use 2% error for $|\Delta m_{31}^2|$ and $\sin^2 2\theta_{23}$, which can be achieved in future long baseline experiments [3]. For $\sigma(\sin^2 2\theta_{13})$ we use 0.02 [24].

Our χ^2 is thus marginalized over the three parameters $\sin^2 2\theta_{13}$, $\sin^2 2\theta_{23}$ and $|\Delta m_{31}^2|$ in order to determine χ_{min}^2 which shows how different are the predictions of the “wrong hierarchy” from those of the “true hierarchy”. “Wrong hierarchy” is then taken to be ruled out at $p\sigma$ if $\chi_{\text{min}}^2 \geq p^2$ for all allowed values of θ_{13} , θ_{23} and $|\Delta m_{31}^2|$.

In our calculations, we took the density profile of the earth to be the PREM profile. There are, of course, some uncertainties in the values of the densities given in this profile. We checked that a 10% change in the density leads to a negligible change (less than 5% change) in the minimum χ^2 . Therefore, we have not taken the uncertainties in the density profile into account explicitly.

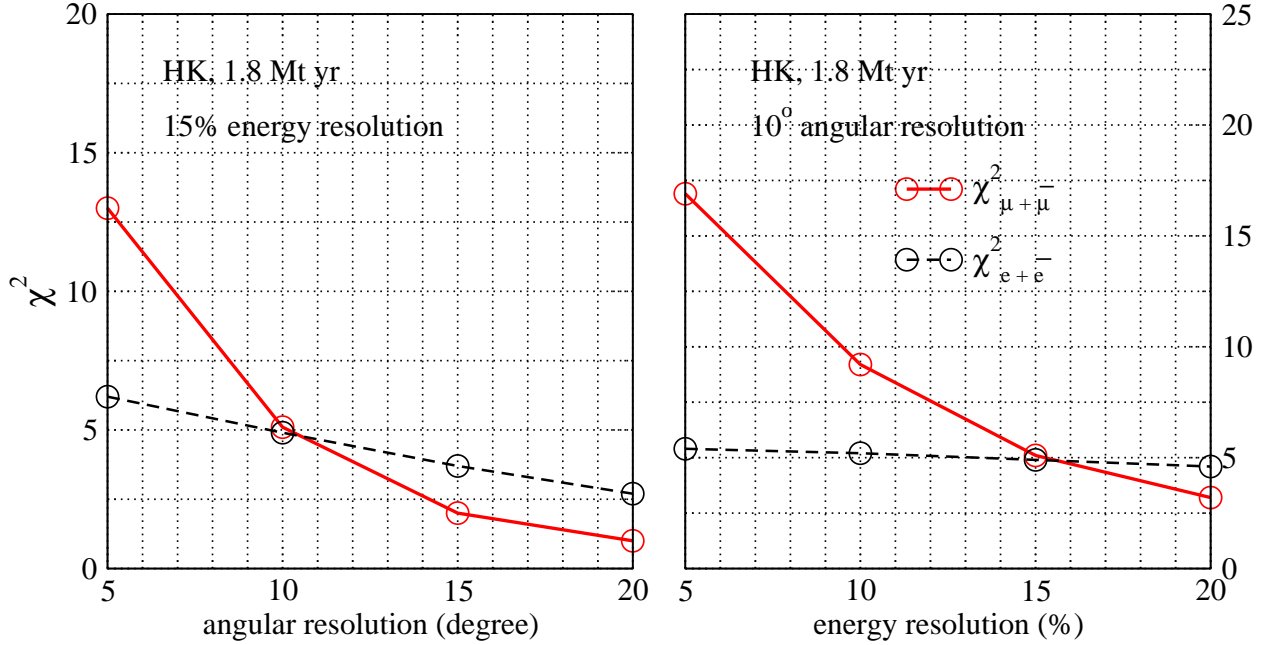


Figure 5: Values of fixed parameter χ^2 versus angular resolution (left panel) and energy resolution (right panel) for HK (1.8 Mt yr). Plots are given separately for $\chi^2_{\mu+\bar{\mu}}$ and $\chi^2_{e+\bar{e}}$. For the left panel, an energy resolution of 15% is assumed, whereas for the right panel, an angular resolution of 10° is assumed. No marginalization over neutrino parameters is done.

5 Results

The ability of an atmospheric neutrino detector to resolve the hierarchy depends on various factors. We study the effect of these different factors by computing the χ^2 as a function of (a) energy and angular resolution of the detector and (b) $\sin^2 2\theta_{13}$, which controls the matter effects.

In studying (a) the same values of the neutrino parameters, $|\Delta m_{31}^2|$, $\sin^2 2\theta_{23}$ and $\sin^2 2\theta_{13}$, are used in computing both N_{ij}^{ex} and N_{ij}^{th} . In studying (b) we marginalize over these parameters.

For HK, the overall sensitivity is taken to be the sum of χ^2 values for the muon and electron event rates and hence, the total $\chi^2 = \chi^2_{\mu+\bar{\mu}} + \chi^2_{e+\bar{e}}$.

For the INO analysis, the μ^- and μ^+ event rate are separately used to compute the χ^2 sensitivity to the hierarchy. The overall sensitivity is taken to be the sum of χ^2 values for the μ^- and μ^+ event rates. Hence, for INO, the total $\chi^2 = \chi^2_{\mu^-} + \chi^2_{\mu^+}$.

5.1 Megaton water Čerenkov detectors

We first discuss our results for megaton water Čerenkov detectors.

The left and right panels of Figure 5 give the values of χ^2_{pull} from Eq. 26 for muon events ($\chi^2_{\mu+\bar{\mu}}$) and for electron events ($\chi^2_{e+\bar{e}}$) as a function of angular and energy resolution respectively. In this figure all neutrino parameters are kept fixed in both N^{th} and N^{ex} . Since the

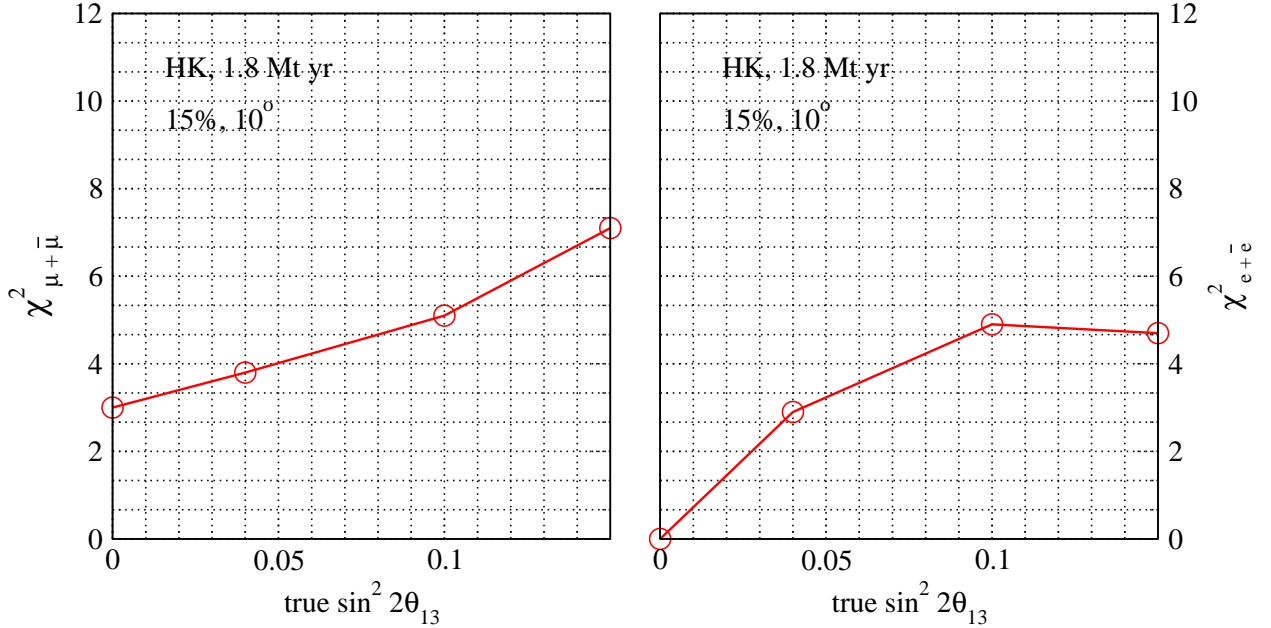


Figure 6: Values of fixed parameter χ^2 versus the input (true) value of $\sin^2 2\theta_{13}$ for HK (1.8 Mt yr), assuming **NH** to be the true hierarchy. Left panel shows $\chi^2_{\mu+\bar{\mu}}$ and right panel shows $\chi^2_{e+\bar{e}}$. An energy resolution of 15% and an angular resolution of 10° are assumed. No marginalization over neutrino parameters is done.

number of muon events is expected to be more than that of the electron events, naively one would expect better hierarchy discrimination in the muon channel. We find that this indeed is the case when the energy and angular resolutions are very good. But with worsening energy and angular resolutions, the hierarchy resolving power of electron events becomes comparable to that of muon events. This is primarily because the contribution to the muon events comes from the probability $P_{\mu\mu}$ and $P_{e\mu}$ whereas for electron events it is from $P_{\mu e}$ and P_{ee} . As is seen from the Figures 1 and 2, the matter effects in $P_{\mu\mu}$ are generally smaller than those in $P_{\mu e}$ and P_{ee} . Also, the matter induced change in $P_{\mu e}$ and P_{ee} is consistently of the same sign over all the relevant ranges in energy and pathlength, while the matter induced change in $P_{\mu\mu}$ is oscillatory for longer baselines. Worsening resolutions thus have a stronger effect on muon events, and, over-riding their statistical advantage, lead to $\chi^2_{\mu+\bar{\mu}} \leq \chi^2_{e+\bar{e}}$.

Figure 6 and Figure 7 give the values of the fixed parameter $\chi^2_{\mu+\bar{\mu}}$ and $\chi^2_{e+\bar{e}}$ as functions of the true value of $\sin^2 2\theta_{13}$. In Figure 6, **NH** is assumed to be the true hierarchy, whereas in Figure 7, **IH** is assumed to be the true hierarchy. The χ^2 values in the two cases are quite close, as one would expect. Since θ_{13} drives the matter effects, it is no surprise that the χ^2 is larger for larger values of θ_{13} . It is interesting to examine the limit where θ_{13} goes to zero for electron and muon events. For the former, one needs to recall that the relevant analytical expressions for P_{ee} and $P_{e\mu}$ in matter are those which are exact in $\Delta m_{21}^2/\Delta m_{31}^2$ and accurate to first order in $\sin^2 2\theta_{13}$ [47–50]. The leading order term in this expansion is devoid of any hierarchy sensitivity, while the term to first order in $\sin^2 2\theta_{13}$ is zero. Thus we expect χ^2 to go to zero in this limit for electron events, and this is borne out by the right panels of both Figure 6 and Figure 7. However, we see from the left panels of these figures that at $\theta_{13} = 0$ the muon events have non-zero χ^2 . The muon disappearance probability in case of $\theta_{13} = 0$

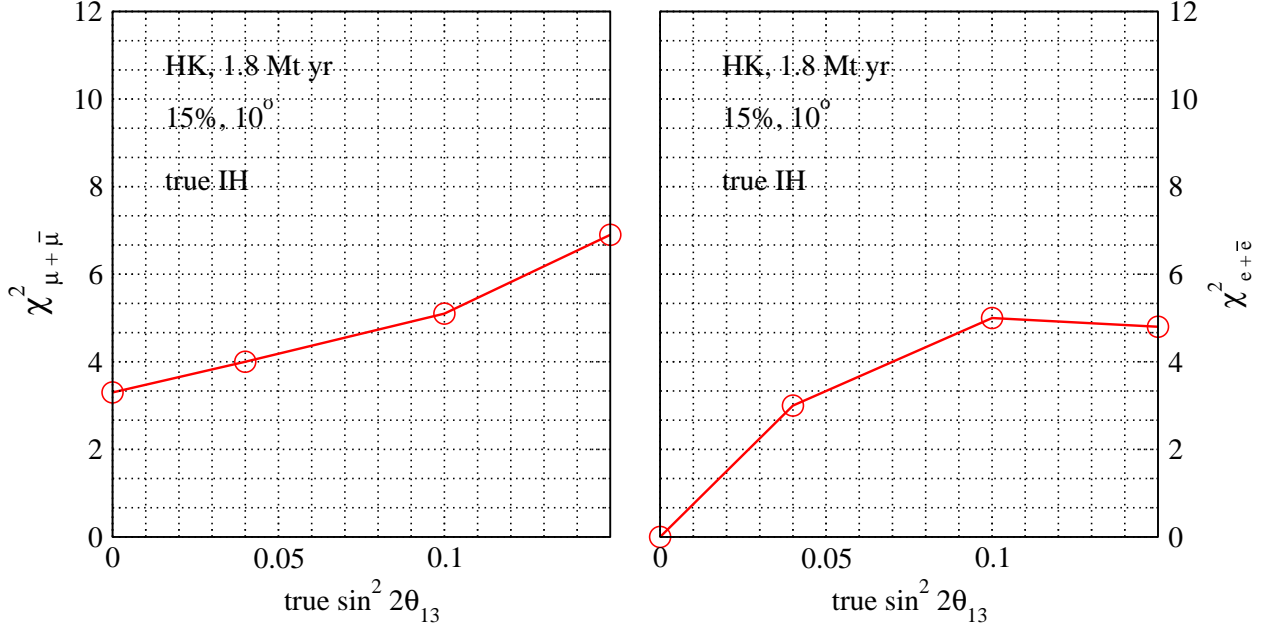


Figure 7: Values of fixed parameter χ^2 versus the input (true) value of $\sin^2 2\theta_{13}$ for HK (1.8 Mt yr), assuming **IH** to be the true hierarchy. Left panel shows $\chi^2_{\mu+\bar{\mu}}$ and right panel shows $\chi^2_{e+\bar{e}}$. An energy resolution of 15% and an angular resolution of 10° are assumed. No marginalization over neutrino parameters is done.

can be expressed as,

$$P_{\mu\mu}^m = \left[1 - \sin^2 2\theta_{23} \sin^2 \left\{ 1.27 (1 - \alpha c_{12}^2) \Delta m_{31}^2 \frac{L}{E} \right\} \right] \quad (28)$$

Here, c_{12} denotes $\cos \theta_{12}$ and α is a dimensionless parameter given by $\alpha = \Delta m_{21}^2 / |\Delta m_{31}^2|$. This gives us

$$P_{\mu\mu}^{\text{NH}} - P_{\mu\mu}^{\text{IH}} = \sin^2 2\theta_{23} \left[\sin^2 \left\{ 1.27(1 + \alpha c_{12}^2) \Delta m_{31}^2 \frac{L}{E} \right\} - \sin^2 \left\{ 1.27(1 - \alpha c_{12}^2) \Delta m_{31}^2 \frac{L}{E} \right\} \right] \quad (29)$$

Thus there is a hierarchy sensitivity due to the term $\alpha = \Delta m_{21}^2 / |\Delta m_{31}^2|$ even for $\theta_{13} = 0$. This is true only if $|\Delta m_{31}^2|$ is known very precisely, permitting the use of the same fixed value of $|\Delta m_{31}^2|$ for normal and inverted hierarchy. For current uncertainties in $|\Delta m_{31}^2|$, marginalization over this parameter leads to a wash out of this sensitivity (as will be shown later). This happens when the values of $|\Delta m_{31}^2|$ in the computation of NH and IH probabilities differ by $2\Delta m_{21}^2 c_{12}^2$ [72, 73]. Hence we would have a non-zero hierarchy sensitivity for $\theta_{13} = 0$ only if the error in the determination of $|\Delta m_{31}^2|$ is less than the magnitude of Δm_{21}^2 .

Another interesting feature visible in Figure 6 and Figure 7 is that for $\sin^2 2\theta_{13} \geq 0.1$, the $\chi^2_{e+\bar{e}}$ flattens out. As emphasized in Section 3, the maximum difference between events in the case of NH and those in the case of IH occurs for energies in the resonance region. At resonance, the matter dependent mixing angle $\theta_{13}^m \simeq \pi/2$, but the matter dependent mass-squared difference $(\Delta m_{31}^2)^m$ takes its minimum value of $\Delta m_{31}^2 \sin 2\theta_{13}$. For intermediate values of θ_{13} , (*i.e.* those that are not tiny but still significantly less than 0.1) this mass-squared

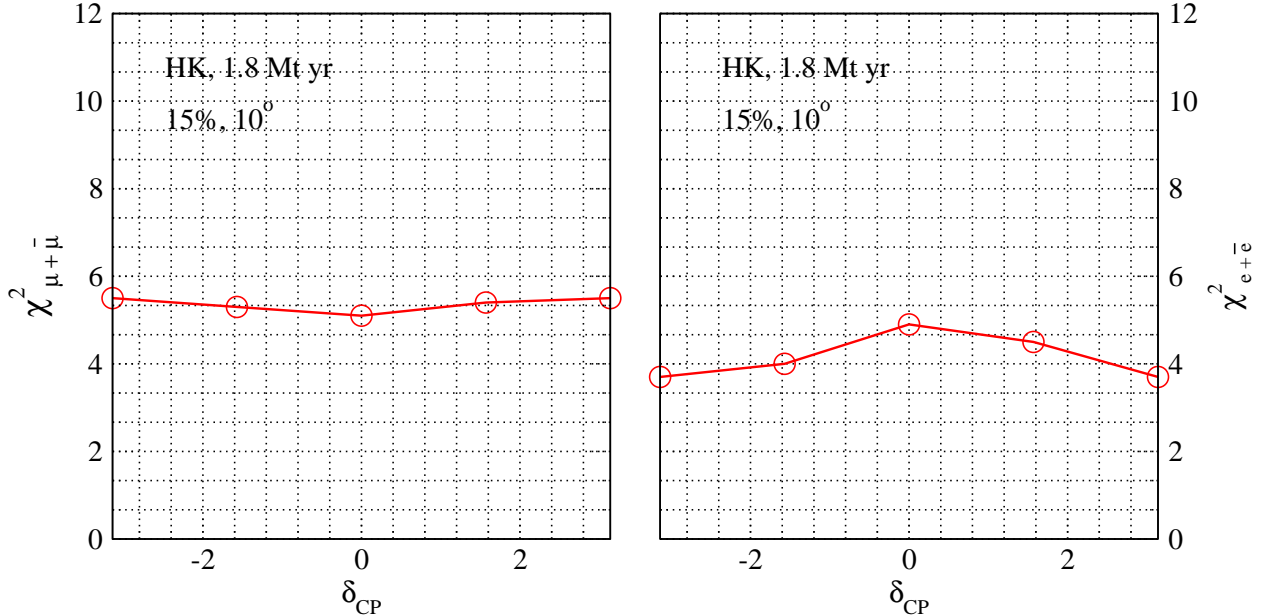


Figure 8: Values of fixed parameter χ^2 versus the input (true) value of δ_{CP} for HK (1.8 Mt yr). Left panel shows $\chi_{\mu+\bar{\mu}}^2$ and right panel shows $\chi_{e+\bar{e}}^2$. An energy resolution of 15% and an angular resolution of 10° are assumed. **NH** is assumed to be true hierarchy. No marginalization over neutrino parameters is done.

difference is too small for the oscillating term in $P_{\mu e}^m$ and P_{ee}^m to come close to unity, even for the largest pathlengths. But for $\sin^2 2\theta_{13} \geq 0.1$, the value of $\Delta m_{31}^2 \sin 2\theta_{13}$ is large enough such that (a) for a large range of pathlengths, $\sin^2(1.27\Delta m_{31}^2 \sin 2\theta_{13} L/E) \lesssim 1$, (b) $P_{\mu e}^m$ is close to its maximum value, and (c) P_{ee}^m is close to its minimum value. Thus, the difference between electron events for NH and those for IH becomes essentially independent of θ_{13} above a certain limit.

Figure 8 gives the values of fixed parameter $\chi_{\mu+\bar{\mu}}^2$ and $\chi_{e+\bar{e}}^2$ as a function of the value of the CP phase δ_{CP} for muon and electron events. This figure shows that the dependence of χ^2 on δ_{CP} is mild. This occurs because the terms containing δ_{CP} in oscillation probabilities are also proportional to Δm_{21}^2 , whose effect on these probabilities is small. Therefore the exact value of δ_{CP} has negligible effect on the hierarchy distinguishing ability of megaton water Čerenkov detectors.

Finally, we present results with marginalization over the neutrino oscillation parameters $|\Delta m_{31}^2|$, $\sin^2 2\theta_{23}$ and $\sin^2 2\theta_{13}$. We add the χ^2 of the muon events ($\chi_{\mu+\bar{\mu}}^2$) and that of the electron events ($\chi_{e+\bar{e}}^2$) and compute the set of χ^2 where all the inputs in N_{ij}^{th} have been varied over their allowed ranges. The minimum of this set, called χ_{min}^2 (Eq. 27), is the quantity characterizing the capability of HK to distinguish the two hierarchies. As explained earlier, this capability is a function of the *true* value of θ_{13} . In Figure 9 we plot the values of the marginalized $\chi_{\mu+\bar{\mu}}^2 + \chi_{e+\bar{e}}^2$ vs the true value of $\sin^2 2\theta_{13}$. The χ^2 curve is flattened for $\sin^2 2\theta_{13} \geq 0.1$ because of the contribution of $\chi_{e+\bar{e}}^2$, which, as discussed earlier, flattens out for higher values of θ_{13} . We find the χ^2 to be ≥ 4 for $\sin^2 2\theta_{13} \geq 0.05$. Thus if D-CHOOZ finds a non-zero value for $\sin^2 2\theta_{13}$, then the combination of muon and electron events at megaton sized water Čerenkov detectors can make a distinction between the two hierarchies at 95% CL over

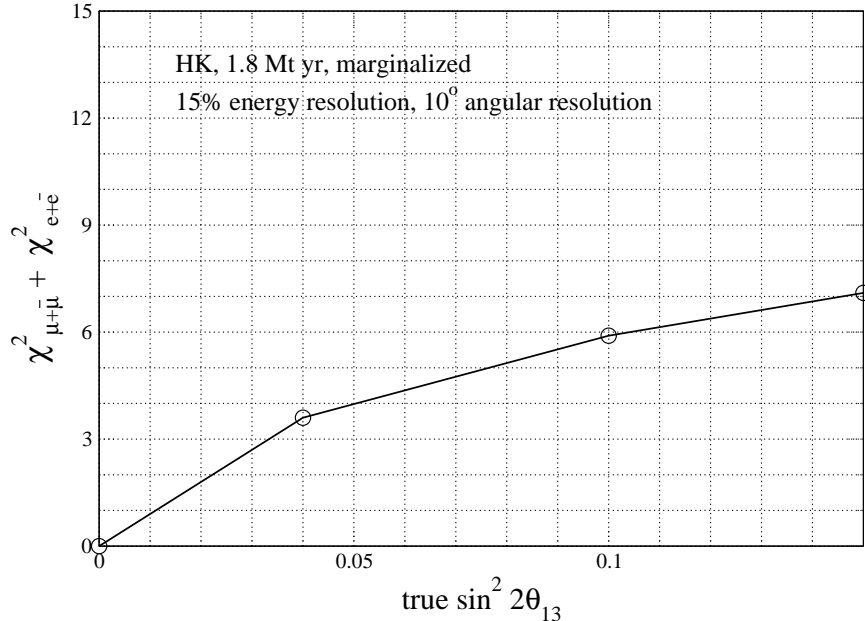


Figure 9: Values of marginalized χ^2 versus the input (true) value of $\sin^2 2\theta_{13}$ for HK (1.8 Mt yr). Shown is the sum of $\chi^2_{\mu+\bar{\mu}}$ and $\chi^2_{e+\bar{e}}$. An energy resolution of 15% and an angular resolution of 10° are assumed.

a ~ 3 year exposure period. Note that, for $\sin^2 2\theta_{13} = 0.05$, the marginalized χ^2 is about half of the fixed parameter χ^2 .

We have not included the backgrounds in our calculations. They will be the same in both “experimental” and “theoretical” spectra and cancel out in the numerator of χ^2_{stat} , as can be seen from Eq. 23. They need to be included in the denominator, which is the sum of “signal” and background events. Thus the denominator will be slightly larger than the computed number N_{ij}^{ex} and χ^2_{stat} will be correspondingly lower. Thus the backgrounds can be adequately taken care of if we divide χ^2_{stat} of muon events by **1.003** and that of electron events by **1.17**. We *have not included* these factors in our calculations but their inclusion makes a very small change in overall χ^2 .

5.2 Magnetized Iron detectors

As stated previously, the iron detector which we use as a prototype (based on the INO design) has a mass of 100 kT and is capable of separating the ν_μ and $\bar{\nu}_\mu$ events, but is insensitive to any electron events. We assume an exposure time of 10 years and first compute the fixed parameter χ^2_{pull} from Eq. 26 and later the marginalized χ^2_{min} (Eq. 27). In both cases, we compute χ^2_μ and $\chi^2_{\bar{\mu}}$ separately and add them. The input values of neutrino parameters are the same ones used in the case of water Čerenkov detectors.

In Figure 10, we plot the fixed parameter $\chi^2_\mu + \chi^2_{\bar{\mu}}$ as a function of angular resolution and energy resolution. From the left panel, we observe that the χ^2 increases sharply (by a factor of 3 or more) if the angular resolution is improved from 10° to 5° . This occurs because the maxima and the minima of $P_{\mu\mu}$ are narrower in width and exhibit a more rapid

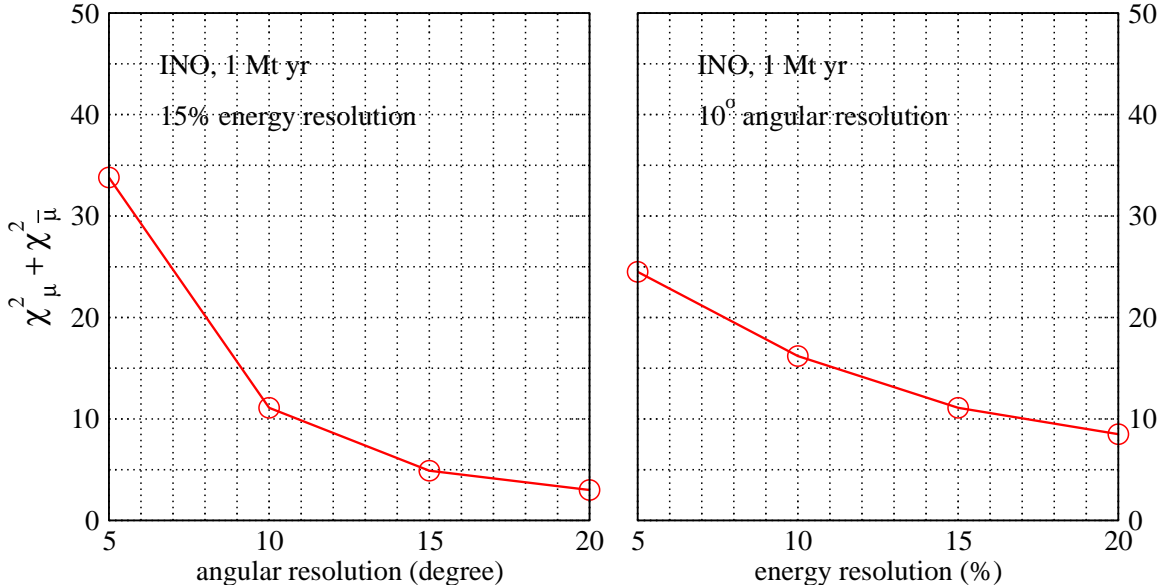


Figure 10: Values of fixed parameter χ^2 versus angular resolution (left panel) and energy resolution (right panel) for INO (1 Mt yr). Shown is the sum of χ_μ^2 and $\chi_{\bar{\mu}}^2$. For the left panel, an energy resolution of 15% is assumed, whereas for the right panel, an angular resolution of 10° is assumed. No marginalization over neutrino parameters is done.

variation (compared to P_{ee}) as the baseline changes, as can be observed in Figures 1 and 2. The improvement in χ^2 due to the improvement in the energy resolution is more modest, as the right panel of Figure 10 shows. Thus it is imperative for such detectors to improve their angular resolution to the best of their ability [38].

In Figure 11, we plot the fixed parameter $\chi_\mu^2 + \chi_{\bar{\mu}}^2$ as a function of the input (*true*) value of $\sin^2 2\theta_{13}$. The left panel assumes NH as the true hierarchy while the right panel assumes IH as the true hierarchy. As in the case of muon events in water Čerenkov detectors, χ^2 increases for increasing values of $\sin^2 2\theta_{13}$. And there is a small non-zero χ^2 for $\theta_{13} = 0$ because of the effect of the non-zero value of Δm_{21}^2 discussed earlier.

Figure 12 demonstrates the variation of $\chi_\mu^2 + \chi_{\bar{\mu}}^2$ with δ_{CP} keeping the other parameters fixed in both NH and IH. As in the case of water Čerenkov detectors, the χ^2 in this case is also insensitive of δ_{CP} .

Finally, we marginalize over the neutrino oscillation parameters $|\Delta m_{31}^2|$, $\sin^2 2\theta_{13}$ and $\sin^2 2\theta_{23}$ and present the marginalized $\chi_\mu^2 + \chi_{\bar{\mu}}^2$ for the magnetized iron detector in Figure 13 as a function of the input value of $\sin^2 2\theta_{13}$. Here again, we find that resolution of mass hierarchy at $\geq 95\%$ C.L. is possible for values of $\sin^2 2\theta_{13} \geq 0.05$. The χ^2 demonstrates a step rise with an increase in θ_{13} which is due to the charge identification capability of magnetized iron calorimeter detectors. For this type of detectors we add the χ^2 from muon events and that from anti-muon events, each of which is a sensitive function of θ_{13} , and therefore the total χ^2 has a large θ_{13} dependence. Note that the χ^2 for $\theta_{13} = 0$ is no longer non-zero due to the marginalization over $|\Delta m_{31}^2|$.

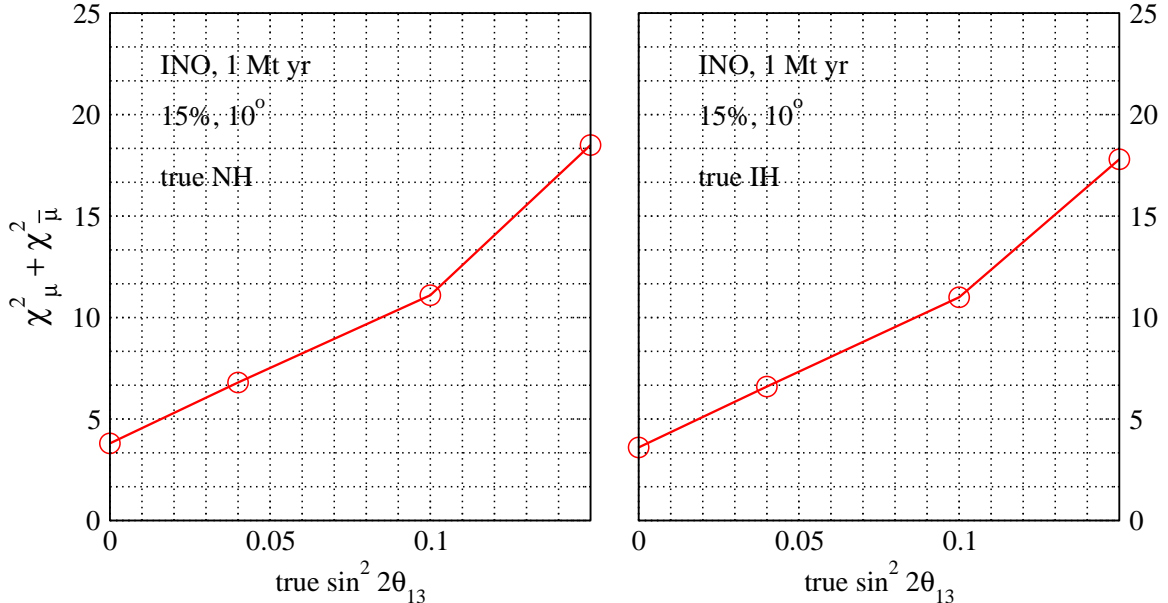


Figure 11: Values of fixed parameter χ^2 versus the input (true) value of $\sin^2 2\theta_{13}$ for INO (1 Mt yr), assuming **NH** (left panel) and **IH** (right panel) to be the true hierarchy. Shown is the sum of χ_μ^2 and $\chi_{\bar{\mu}}^2$. An energy resolution of 15% and an angular resolution of 10° are assumed. No marginalization over neutrino parameters is done.

6 Summary

In this paper, we have studied the hierarchy resolving power of (a) megaton sized water Čerenkov detectors (prototype: **HK**) and (b) magnetized iron detectors (prototype: **INO**).

The first class of detectors has two important advantages: (a) a very large size leading to high statistics and (b) the ability to detect both muon and electron events. However, these detectors are insensitive to the charge of the lepton and therefore one needs to sum over the lepton and antilepton events. The matter effect affects the lepton events for NH and antilepton events for IH, and in the summed event rate these effects can cancel each other. In actual practice however the cancellation is only partial since the neutrino cross section for producing leptons is about 2.5–3 times higher than the corresponding anti-neutrino cross section. This leads to hierarchy sensitivity in these detectors, and despite the above disadvantages, the sheer weight of statistics can lead to significant differences in the signal for the two hierarchies.

For the binned χ^2 analysis of atmospheric neutrino data it is important to include the effect of energy and angular smearing. This effect is more significant for muon events than for electron events. This is because the matter effects in $P_{\mu\mu}$ are generally smaller than those in P_{ee} and $P_{\mu e}$ over the energy and baseline ranges under consideration here. Also, $P_{\mu\mu}$ exhibits an oscillatory behaviour with energy at the longer baseline values (~ 10000 km) which tends to get washed out with smearing. P_{ee} and $P_{\mu e}$, on the other hand, have a significant matter effect over a broad range of energies and pathlengths, which is less affected by smearing. Thus the electron events gain in significance, and the cumulative effect from a number of bins adds up to create a large difference between the hierarchies, even though the electron neutrino flux

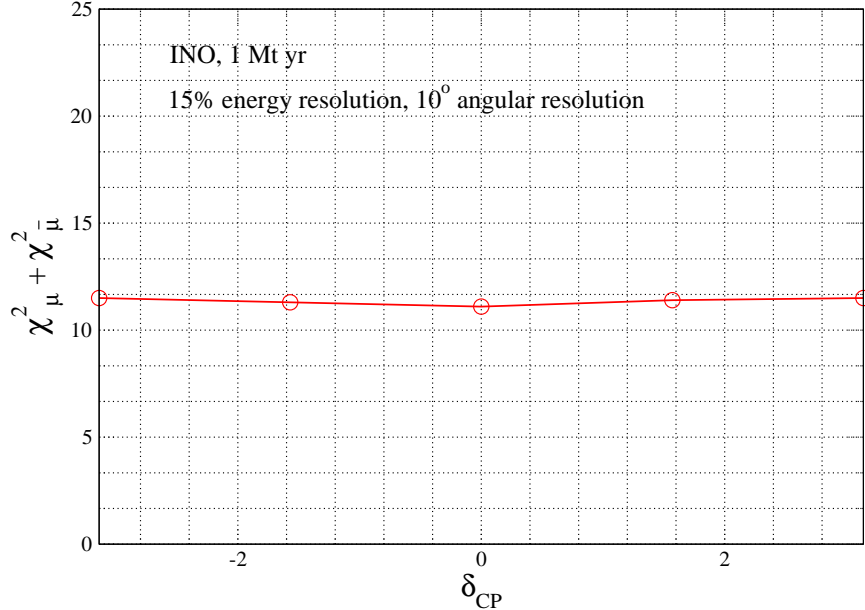


Figure 12: Values of fixed parameter χ^2 versus the input (true) value of δ_{CP} for INO (1 Mt yr). Shown is the sum of χ_μ^2 and $\chi_{\bar{\mu}}^2$. An energy resolution of 15% and an angular resolution of 10° are assumed. **NH** is assumed to be true hierarchy. No marginalization over neutrino parameters is done.

$\sin^2 2\theta_{13}$	$\chi_{\mu+\bar{\mu}}^2 + \chi_{e+\bar{e}}^2$ (HK)	$\chi_\mu^2 + \chi_{\bar{\mu}}^2$ (INO)
0.0	0.0	0.0
0.04	3.6	4.5
0.10	5.9	9.6
0.15	7.1	16.9

Table 4: Values of total marginalized χ^2 with pull and priors, for HK (1.8 Mt yr) and INO (1 Mt yr).

is only about half of the muon neutrino flux. Together, the differences induced in μ -like and e-like events lead to a 2σ signal for neutrino mass hierarchy for $\sin^2 2\theta_{13} \approx 0.04$ for a moderate exposure time of 3.3 years. For larger exposure times, it is possible to determine hierarchy at a higher statistical significance.

Magnetized iron calorimeter detectors, on the other hand, are sensitive only to muons. But the magnetic field endows them with charge identification capability. Therefore one can collect the muon and the anti-muon events separately and compute the χ^2 for each type of events and then add these. Thus the hierarchy sensitivity is considerably enhanced as compared to water Čerenkov detectors, and similar statistical significance can be achieved with smaller statistics.

In Table 4 we compare the χ^2 sensitivity of both type of detectors for different values of $\sin^2 2\theta_{13}$. We find that an exposure of about 2 Mt yr for water Čerenkov and 1 Mt yr for magnetized iron detectors can resolve the matter hierarchy at 95% C.L. or better, provided

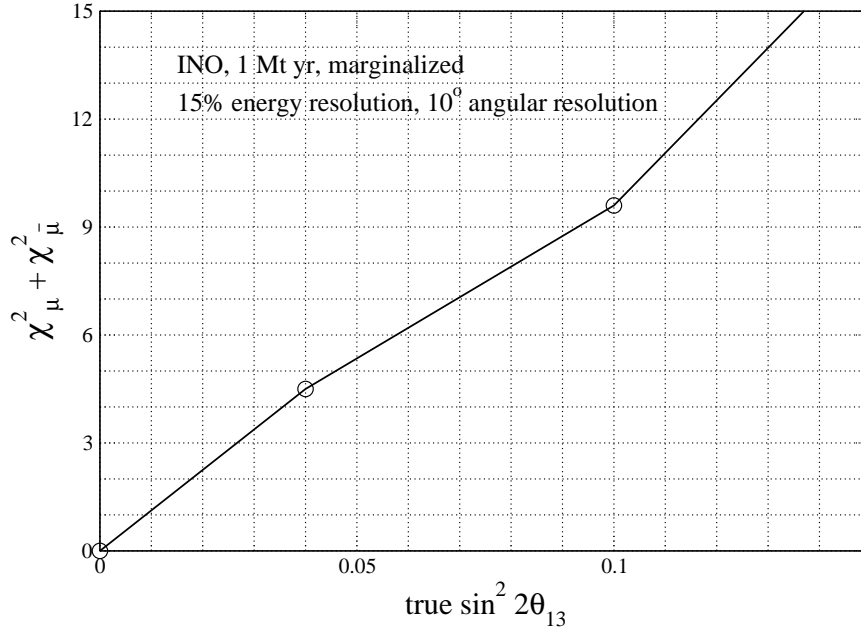


Figure 13: Values of marginalized χ^2 versus the input (true) value of $\sin^2 2\theta_{13}$ for INO (1 Mt yr). Shown is the sum of χ_μ^2 and $\chi_{\bar{\mu}}^2$. An energy resolution of 15% and an angular resolution of 10° are assumed.

$\sin^2 2\theta_{13} \geq 0.05$. This table and Figures 9 and 13 summarize our main results, where χ_{\min}^2 is plotted versus the input value of $\sin^2 2\theta_{13}$. This χ_{\min}^2 incorporates theoretical, statistical and systematic errors, along with smearing over neutrino energy and direction and also marginalization over the allowed ranges of neutrino parameters. These figures as well as the table show that the variation of χ^2 with increasing $\sin^2 2\theta_{13}$ for water Čerenkov detectors is significantly flatter as compared to that for magnetized iron calorimeter detectors. This is due to (a) The contribution of $\chi_{e+\bar{e}}^2$ in the χ^2 for HK, which flattens out for higher values of θ_{13} ; and (b) $\chi_{\mu+\bar{\mu}}^2$ is a relatively less sensitive function of θ_{13} since the addition of muon and anti-muon events partially cancels the θ_{13} dependence in the difference in NH and IH events (Eq. 17). On the other hand, for magnetized iron calorimeter detectors χ^2 is the sum of the χ^2 from muon events and that from anti-muon events and the θ_{13} sensitivity adds constructively in this case.

The χ^2 for muon events exhibits a higher sensitivity to improved angular and energy resolution than do electron events. Hence, there is a dramatic improvement in the hierarchy discrimination capability of magnetized iron detectors with improved angular resolution. The results quoted in the previous paragraph assume a modest energy resolution of 15% and angular resolution of 10° . Increasing the the angular resolution from 10° to 5° dramatically increases the χ^2 by a factor of 3. Improvement in the energy resolution for a magnetized detector leads to a more modest improvement of the χ^2 . Thus it is imperative for these detectors to have good angular resolution if they are to resolve the mass hierarchy at a statistically significant level.

Acknowledgements

We would like to thank S. Choubey for helpful discussions and cross-checking our numerical code. We thank J. Kopp, T. Schwetz and T. Kajita for useful discussions. S.G. was supported by the Alexander von-Humboldt Foundation during a part of this work and would like to thank Max-Planck-Institut for Kernphysik, Heidelberg and Tata Institute of Fundamental Research, Mumbai for hospitality during the final phases of this work. R.G. would like to acknowledge the support and hospitality of the Aspen Center for Physics and the SLAC theory group while the final stages of this work were in progress. S.U.S. would like to thank the theory group at CERN for their hospitality during the finishing stages of this work. S.G. and S.U.S. thank BRNS project number 2006/37/9 (Govt. of India) for partial financial support. S.S. would like to thank the INO collaboration for support. P.M. acknowledges the Weizmann Institute of Science, Israel for financial support. Part of the computational work for this study was carried out at cluster computing facility in the Harish-Chandra Research Institute (<http://www.cluster.mri.ernet.in>).

A Calculation of the normalization constant

In this appendix, we give the procedure for computing the Gaussian resolution function for angular smearing.

The flux distribution in terms of the zenith direction is given as $(d\Phi/d \cos \theta_t)$. Thus the flux per solid angle is given by $(1/2\pi)(d\Phi/d \cos \theta_t)$. The number of events per unit solid angle are given by

$$\frac{dN_\mu}{d\Omega_t} = \frac{1}{2\pi} \left[\left(\frac{d\Phi}{d \cos \theta_t} \right)_\mu P_{\mu\mu} + \left(\frac{d\Phi}{d \cos \theta_t} \right)_e P_{e\mu} \right] \sigma_{CC} \quad (A1)$$

Even though the left hand side says Ω_t , this quantity is independent of ϕ_t . This plays a key role in later calculation. In the above expression, the disappearance and appearance probabilities are functions of neutrino travel distance and hence of θ_t . In addition, they and the cross section are also functions of neutrino energy, which we will not explicitly consider in this discussion.

Now consider a unit sphere with two nearby points whose coordinates are (θ_t, ϕ_t) and (θ_m, ϕ_m) . The distance between them is given by

$$ds^2 = (\theta_t - \theta_m)^2 + \sin^2 \theta_t (\phi_t - \phi_m)^2 \quad (A2)$$

Let $\Delta\theta$ be the uncertainty in the determination of the neutrino direction, which is given by the point (θ_t, ϕ_t) . Then the smearing factor for the solid angle is

$$R(\Omega_t, \Omega_m) = N \exp \left[- \frac{(\theta_t - \theta_m)^2 + \sin^2 \theta_t (\phi_t - \phi_m)^2}{2 (\Delta\theta)^2} \right] \quad (A3)$$

Here, the normalization factor $N = 1/A(\theta_t)$, where $A(\theta_t)$ is the area of the Gaussian for each value of θ_t . Since the Gaussians at the edges are truncated, this causes a fall in the area of the

side bins if the normalization factor used is $\sqrt{2\pi}\sigma$ (the area of a full Gaussian). We require the total event number to be preserved when the range of $\cos\theta_m$ is the full range (-1 to +1), since any value of $\cos\theta$ outside this range is unphysical and hence no events should come in or be thrown out. So, the normalization has to be by the actual area of each Gaussian.

For each value of θ_t , the Gaussian area is given by

$$A(\theta_t) = \int_{-\pi}^{\pi} d\phi_m \int_0^{\pi} d\theta_m \sin\theta_m \exp\left[-\frac{(\theta_t - \theta_m)^2 + \sin^2\theta_t (\phi_t - \phi_m)^2}{2(\Delta\theta)^2}\right] \quad (\text{A4})$$

On computing the ϕ_m integral, using the same method described below in Eq. A8-A10, we get

$$N(\theta_t) = \frac{1}{A(\theta_t)} = \left[\int_{-1}^1 d\cos\theta_m \exp\left[-\frac{(\theta_t - \theta_m)^2}{2(\Delta\theta)^2}\right] \frac{\sqrt{2\pi}\Delta\theta}{\sin\theta_t} \right]^{-1} \quad (\text{A5})$$

Combining the smearing factor from Eq. 21 with the distribution in true angles coming from Eq. A1, and integrating over ϕ_t and θ_t we get the distribution in measured angles

$$\frac{dN_\mu}{d\Omega_m} = \int \left(\frac{dN_\mu}{d\Omega_t} \right) R(\Omega_t, \Omega_m) d\Omega_t \quad (\text{A6})$$

where $d\Omega_t = d\theta_t \sin\theta_t d\phi_t$. In the above equation, ϕ_t appears only in the smearing factor and it appears only as $(\phi_t - \phi_m)^2$. We can define this as $\tilde{\phi}_m^2$ so that the integrand is completely independent of ϕ_t and that integration is trivial. Thus the distribution in measured angles is given by

$$\frac{dN_\mu}{d\Omega_m} = (2\pi) \int_0^\pi \left(\frac{dN_\mu}{d\Omega_t} \right) R(\Omega_t, \Omega_m) \sin\theta_t d\theta_t \quad (\text{A7})$$

Now we do the integral over ϕ_m so that we have the distribution over $\cos\theta_m$ on LHS and $\cos\theta_t$ on RHS. On RHS, only the smearing factor $R(\Omega_t, \Omega_m)$ depends on ϕ_m . Thus doing the ϕ_m integral we get

$$\int \frac{dN_\mu}{d\Omega_m} d\phi_m = 2\pi \int_{-\pi}^{\pi} \int_0^{\pi} \frac{dN_\mu}{d\Omega_t} N(\theta_t) \exp\left[-\frac{(\theta_t - \theta_m)^2 + \sin^2\theta_t (\phi_t - \phi_m)^2}{2(\Delta\theta)^2}\right] \sin\theta_t d\theta_t d\phi_m \quad (\text{A8})$$

Changing variable to $\tilde{\phi}_m = \phi_m - \phi_t$, we get

$$\int \frac{dN_\mu}{d\Omega_m} d\phi_m = 2\pi \int_{-\pi}^{\pi} \int_0^{\pi} \frac{dN_\mu}{d\Omega_t} N(\theta_t) \exp\left[-\frac{(\theta_t - \theta_m)^2 + \sin^2\theta_t (\tilde{\phi}_m)^2}{2(\Delta\theta)^2}\right] \sin\theta_t d\theta_t d\tilde{\phi}_m \quad (\text{A9})$$

In doing the ϕ_m ($\tilde{\phi}_m$) integration, we extend the limits of integration from $\pm\pi$ to $\pm\infty$. This leads to negligible error because the Gaussian falls off very steeply. After the integration, we get

$$\frac{dN_\mu}{d\cos\theta_m} = 2\pi \int_0^\pi \frac{dN_\mu}{d\Omega_t} N(\theta_t) \exp\left[-\frac{(\theta_t - \theta_m)^2}{2(\Delta\theta)^2}\right] \sin\theta_t d\theta_t \sqrt{2\pi}\Delta\theta \frac{1}{\sin\theta_t} \quad (\text{A10})$$

We can cancel one factor of $\sin \theta_t$ on the RHS. On substituting for $N(\theta_t)$ from Eq. A5 and $dN_\mu/d\Omega_t$ from Eq. A1, we get the binned distribution in $\cos \theta_m$ to be

$$\begin{aligned}
dN_\mu &= \int d\theta_t \frac{[(d\Phi/d \cos \theta_t)_\mu P_{\mu\mu} + (d\Phi/d \cos \theta_t)_e P_{e\mu}] \sigma_{CC} \int_{\text{bin}} d \cos \theta_m \exp \left[-\frac{(\theta_t - \theta_m)^2}{2 (\Delta\theta)^2} \right] \sqrt{2\pi} \Delta\theta}{\int_{-1}^1 d \cos \theta_m \exp \left[-\frac{(\theta_t - \theta_m)^2}{2 (\Delta\theta)^2} \right] \frac{\sqrt{2\pi} \Delta\theta}{\sin \theta_t}} \\
&= \int d\theta_t \frac{[(d\Phi/d \cos \theta_t)_\mu P_{\mu\mu} + (d\Phi/d \cos \theta_t)_e P_{e\mu}] \sigma_{CC} \sin \theta_t \int_{\text{bin}} d \cos \theta_m \exp \left[-\frac{(\theta_t - \theta_m)^2}{2 (\Delta\theta)^2} \right]}{\int_{-1}^1 d \cos \theta_m \exp \left[-\frac{(\theta_t - \theta_m)^2}{2 (\Delta\theta)^2} \right]}
\end{aligned} \tag{A11}$$

References

- [1] T. Schwetz, Phys. Scripta **T127**, 1 (2006), [hep-ph/0606060](#).
- [2] K. Nakamura, Front. Phys. **35**, 359 (2000).
- [3] Y. Itow *et al.*, Nucl. Phys. Proc. Suppl. **111**, 146 (2001), [hep-ex/0106019](#).
- [4] C. K. Jung (1999), [hep-ex/0005046](#).
- [5] A. de Bellefon *et al.* (2006), [hep-ex/0607026](#).
- [6] M. S. Athar *et al.* (INO) (2006), a Report of the INO Feasibility Study. Updated from the earlier Interim Report of May 1, 2005.
- [7] H. Minakata and H. Nunokawa, JHEP **10**, 001 (2001), [hep-ph/0108085](#).
- [8] V. Barger, D. Marfatia, and K. Whisnant, Phys. Rev. **D65**, 073023 (2002), [hep-ph/0112119](#).
- [9] P. Huber and W. Winter, Phys. Rev. **D68**, 037301 (2003), [hep-ph/0301257](#).
- [10] A. Y. Smirnov (2006), [hep-ph/0610198](#).
- [11] R. Gandhi and W. Winter, Phys. Rev. **D75**, 053002 (2007), [hep-ph/0612158](#).
- [12] H. Minakata and S. Uchinami (2006), [hep-ph/0612002](#).
- [13] V. Barger, D. Marfatia, and K. Whisnant, Phys. Lett. **B560**, 75 (2003), [hep-ph/0210428](#).
- [14] J. Burguet-Castell, M. B. Gavela, J. J. Gomez-Cadenas, P. Hernandez, and O. Mena, Nucl. Phys. **B646**, 301 (2002), [hep-ph/0207080](#).
- [15] Y. F. Wang, K. Whisnant, Z.-h. Xiong, J. M. Yang, and B.-L. Young (VLBL Study Group H2B-4), Phys. Rev. **D65**, 073021 (2002), [hep-ph/0111317](#).

- [16] K. Whisnant, J. M. Yang, and B.-L. Young, Phys. Rev. **D67**, 013004 (2003), hep-ph/0208193.
- [17] P. Huber, M. Lindner, T. Schwetz, and W. Winter, Nucl. Phys. **B665**, 487 (2003), hep-ph/0303232.
- [18] A. Donini, E. Fernandez-Martinez, P. Migliozzi, S. Rigolin, and L. Scotto Lavina (2004), hep-ph/0406132.
- [19] O. Mena, S. Palomares-Ruiz, and S. Pascoli, Phys. Rev. **D73**, 073007 (2006), hep-ph/0510182.
- [20] M. Ishitsuka, T. Kajita, H. Minakata, and H. Nunokawa, Phys. Rev. **D72**, 033003 (2005), hep-ph/0504026.
- [21] Y. Hayato (T2K), Nucl. Phys. Proc. Suppl. **143**, 269 (2005).
- [22] Y. G. Kudenko (T2K) (2005), prepared for 9th ICATPP Conference on Astroparticle, Particle, Space Physics, Detectors and Medical Physics Applications, Villa Erba, Como, Italy, 17-21 Oct 2005.
- [23] D. S. Ayres *et al.* (NOvA) (2004), hep-ex/0503053.
- [24] P. Huber, M. Lindner, M. Rolinec, T. Schwetz, and W. Winter, Phys. Rev. **D70**, 073014 (2004), hep-ph/0403068.
- [25] H. Minakata, H. Nunokawa, and S. J. Parke, Phys. Rev. **D68**, 013010 (2003), hep-ph/0301210.
- [26] O. Mena and S. J. Parke, Phys. Rev. **D70**, 093011 (2004), hep-ph/0408070.
- [27] O. Mena and S. J. Parke, Phys. Rev. **D72**, 053003 (2005), hep-ph/0505202.
- [28] S. K. Agarwalla, S. Choubey, and A. Raychaudhuri, Nucl. Phys. **B771**, 1 (2007), hep-ph/0610333.
- [29] E. K. Akhmedov, M. Maltoni, and A. Y. Smirnov, Phys. Rev. Lett. **95**, 211801 (2005), hep-ph/0506064.
- [30] A. Cervera *et al.*, Nucl. Phys. **B579**, 17 (2000), hep-ph/0002108.
- [31] C. Albright *et al.*, Nucl. Phys. **B547**, 21 (2000), hep-ex/0008064, `{\protect\protect\protect\edef0T1{0T1}\let\enc@update\relax\protect`
- [32] M. Freund, P. Huber, and M. Lindner, Nucl. Phys. **B615**, 331 (2001), hep-ph/0105071.
- [33] S. Choubey (2006), hep-ph/0609182.
- [34] R. Gandhi, P. Ghoshal, S. Goswami, P. Mehta, and S. Uma Sankar, Phys. Rev. **D73**, 053001 (2006), hep-ph/0411252.

- [35] M. C. Banuls, G. Barenboim, and J. Bernabeu, Phys. Lett. **B513**, 391 (2001), [hep-ph/0102184](#).
- [36] J. Bernabeu, S. Palomares-Ruiz, A. Perez, and S. T. Petcov, Phys. Lett. **B531**, 90 (2002), [hep-ph/0110071](#).
- [37] D. Indumathi and M. V. N. Murthy, Phys. Rev. **D71**, 013001 (2005), [hep-ph/0407336](#).
- [38] S. T. Petcov and T. Schwetz, Nucl. Phys. **B740**, 1 (2006), [hep-ph/0511277](#).
- [39] A. Samanta (2006), [hep-ph/0610196](#).
- [40] P. Huber, M. Maltoni, and T. Schwetz, Phys. Rev. **D71**, 053006 (2005), [hep-ph/0501037](#).
- [41] J. E. Campagne, M. Maltoni, M. Mezzetto, and T. Schwetz (2006), [hep-ph/0603172](#).
- [42] A. Donini *et al.* (2007), [hep-ph/0703209](#).
- [43] S. Choubey and P. Roy, Phys. Rev. **D73**, 013006 (2006), [hep-ph/0509197](#).
- [44] D. Indumathi, M. V. N. Murthy, G. Rajasekaran, and N. Sinha, Phys. Rev. **D74**, 053004 (2006), [hep-ph/0603264](#).
- [45] R. Gandhi, P. Ghoshal, S. Goswami, P. Mehta, and S. Uma Sankar (2005), [hep-ph/0506145](#).
- [46] A. M. Dziewonski and D. L. Anderson, Phys. Earth and Planet Int. **25**, 297 (1981).
- [47] M. Freund, Phys. Rev. **D64**, 053003 (2001), [hep-ph/0103300](#).
- [48] E. K. Akhmedov, R. Johansson, M. Lindner, T. Ohlsson, and T. Schwetz, JHEP **04**, 078 (2004), [hep-ph/0402175](#).
- [49] K. Kimura, A. Takamura, and H. Yokomakura, Phys. Lett. **B537**, 86 (2002), [hep-ph/0203099](#).
- [50] A. Takamura and K. Kimura, JHEP **01**, 053 (2006), [hep-ph/0506112](#).
- [51] S. P. Mikheyev and A. Y. Smirnov, Prog. Part. Nucl. Phys. **23**, 41 (1989).
- [52] L. Wolfenstein, Phys. Rev. **D17**, 2369 (1978).
- [53] E. K. Akhmedov, Sov. J. Nucl. Phys. **47**, 301 (1988).
- [54] S. K. Agarwalla, S. Choubey, S. Goswami, and A. Raychaudhuri (2006), [hep-ph/0611233](#).
- [55] R. Gandhi, P. Ghoshal, S. Goswami, P. Mehta, and S. Uma Sankar, Phys. Rev. Lett. **94**, 051801 (2005), [hep-ph/0408361](#).
- [56] S. T. Petcov, Phys. Lett. **B434**, 321 (1998), [hep-ph/9805262](#).

- [57] E. K. Akhmedov, A. Dighe, P. Lipari, and A. Y. Smirnov, Nucl. Phys. **B542**, 3 (1999), [hep-ph/9808270](#).
- [58] E. K. Akhmedov, Nucl. Phys. **B538**, 25 (1999), [hep-ph/9805272](#).
- [59] A. Rubbia, Nucl. Phys. Proc. Suppl. **147**, 103 (2005), [hep-ph/0412230](#).
- [60] T. Kajita, *For plots of efficiency.*, private Communication.
- [61] Y. Ashie *et al.* (Super-Kamiokande), Phys. Rev. Lett. **93**, 101801 (2004), [hep-ex/0404034](#).
- [62] M. Ishitsuka, *L/E analysis of the atmospheric neutrino data from Super-Kamiokande*, Ph.D. thesis, Tokyo University (2004).
- [63] Y. Ashie *et al.* (Super-Kamiokande), Phys. Rev. **D71**, 112005 (2005), [hep-ex/0501064](#).
- [64] S. K. Agarwalla, A. Raychaudhuri, and A. Samanta (2005), [hep-ph/0505015](#).
- [65] P. Huber, M. Lindner, and W. Winter, Comput. Phys. Commun. **167**, 195 (2005), <http://www.ph.tum.de/~globes>, [hep-ph/0407333](#).
- [66] M. D. Messier, *Evidence for neutrino mass from observations of atmospheric neutrinos with Super-Kamiokande*, Ph.D. thesis, Boston University (1999).
- [67] E. A. Paschos and J. Y. Yu, Phys. Rev. **D65**, 033002 (2002), [hep-ph/0107261](#).
- [68] M. Honda, T. Kajita, K. Kasahara, and S. Midorikawa, Phys. Rev. **D70**, 043008 (2004), [astro-ph/0404457](#).
- [69] M. C. Gonzalez-Garcia and M. Maltoni, Phys. Rev. **D70**, 033010 (2004), [hep-ph/0404085](#).
- [70] G. L. Fogli, E. Lisi, A. Marrone, D. Montanino, and A. Palazzo, Phys. Rev. **D66**, 053010 (2002), [hep-ph/0206162](#).
- [71] G. L. Fogli, E. Lisi, A. Marrone, and D. Montanino, Phys. Rev. **D67**, 093006 (2003), [hep-ph/0303064](#).
- [72] A. de Gouvea, J. Jenkins, and B. Kayser, Phys. Rev. **D71**, 113009 (2005), [hep-ph/0503079](#).
- [73] A. de Gouvea and W. Winter, Phys. Rev. **D73**, 033003 (2006), [hep-ph/0509359](#).